

Anthropogenic contributions to slow warming over 1998-2012

Xuanming Su^{1,*}, Hideo Shiogama², Katsumasa Tanaka^{2,3},
Kaoru Tachiiri⁴, Tomohiro Hajima⁴, Michio Watanabe⁴,
Michio Kawamiya⁴, Kiyoshi Takahashi¹ & Tokuta Yokohata²

¹Social Systems Division, National Institute for Environmental Studies(NIES), Tsukuba, Japan

²Earth System Division, National Institute for Environmental Studies (NIES), Tsukuba, Japan

³Laboratoire des Sciences du Climat et de l'Environnement (LSCE), IPSL, CEA/CNRS/UVSQ, Université Paris-Saclay, Gif-sur-Yvette, France

⁴Research Institute for Global Change/Research Centre for Environmental Modelling and Application, Japan Agency for Marine-Earth Science and Technology (JAMSTEC), Yokohama, Japan

*To whom correspondence should be addressed; E-mail: su.xuanming@nies.go.jp.

The observed global mean surface temperature increase from 1998 to 2012 was slower than that since 1951. The relative contributions of all relevant factors including climate forcings, however, have not been comprehensively analyzed. Using a reduced-complexity climate model and an observationally constrained statistical model, we find that La Niña cooling and a descending solar cycle contributed approximately 50% and 26% of the total warming slowdown during 1998-2012 compared to 1951-2012. Furthermore, reduced ozone-depleting substances and methane accounted for roughly a quarter of the total warm-

ing slowdown, which can be explained by changes in atmospheric concentrations. We identify that human factors played an important role in slowing global warming during 1998-2012, shedding light on the evidence for controlling global warming by reducing greenhouse gas emissions.

Introduction

Observations implied a slow warming (SW) in global mean temperature change (ΔT) from 1998 to 2012 compared to the warming from 1951 to 2012, despite the rapid growth in greenhouse gas (GHG) emissions during the same period (1). The warming difference of decadal trends (DDT), that is, the decadal trend of 1998-2012 minus that of 1951-2012, indicated a negative trend. Newer temperature records with updated sea surface temperature (SST) datasets and the infilling of missing data in places such as the Arctic showed greater positive trends, implying that the slowing was not as severe as previously thought (2). For example, the latest Met Office Hadley Centre/Climatic Research Unit global surface temperature anomalies, version 5 (HadCRUT5), used by default in this study, showed an apparently less negative DDT (-0.011 °C/decade) compared to the older version of HadCRUT4.6 (-0.055 °C/decade). Such a slowing trend may differ among independent observations (fig. S1). Nonetheless, there is no doubt that SW does exist (3). The Sixth Assessment Report (AR6) of the Intergovernmental Panel on Climate Change (IPCC) referred to this phenomenon as a temporary event (4), primarily due to internal variability (5–10) and natural forcings such as volcanic and solar irradiance (3, 11–16). The strengths of internal variability or natural forcings, however, are uncertain (1, 4, 17, 18). Reductions in methane and ozone-depleting substances (ODS) (19, 20) or stratospheric water vapour (21) may also have contributed, but their respective impacts have not been explicitly calculated. Furthermore, SW cannot be described by a single factor; rather, it necessitates an integrated influence combining multiple components, such as internal variability,

forcing changes, ocean heat uptake, and insufficient observational coverage (15, 22–25). Quantifications of relative contributions from these individual components are important to interpret the causes of SW.

Physical climate models may insufficiently capture the internal variability or underestimate the response of solar irradiance (3), resulting in a higher-than-observed ΔT during the SW period (4). Statistical models, on the other hand, can capture ΔT variations but strongly depend on the chosen predictors and their time lags and usually use the whole anthropogenic influence as an input (3, 11, 26), hindering further attributions at the emission level. A systematic and reliable assessment of the individual contributing factors to SW has not been conducted to our knowledge. Here, we combined a reduced-complexity model (RCM) used to quantify the ΔT trends caused by individual climate forcings with a statistical regression model to reconcile the causes with the observed ΔT .

Results

Method summary

To attribute anthropogenic and natural ΔT , first, we applied a normalized marginal approach (27–29) to an RCM, the Simple Climate Model for Optimization version 3.3 (SCM4OPT v3.3) (30–33), to quantify the ΔT trends for respective climate forcings (see materials and methods). Second, we used a regression statistical model (3, 11, 26) to decode the impacts of anthropogenic and natural factors. This was a twofold approach: the regression can correct the biases in the magnitude of the simulated ΔT , while the relative contributions of external forcing factors and internal variability to the observed ΔT are resolved. To avoid overfitting, we tested a group of statistical models with different predictors and chose the one with the lowest Bayesian information criterion (BIC) (table S1). The monthly observed ΔT was then modeled as a multiple regression of anthropogenic factors, natural forcings, El Niño and Southern Oscillation (ENSO),

and residuals allowing for errors in simulations and observations (see materials and methods). As a result, we decomposed the observed ΔT into ΔT caused by each anthropogenic factor, such as CO₂, CH₄, N₂O, ODS, other fluorinated gases, aerosols and pollutants, and land use albedo, as well as each natural factor, such as volcanic eruptions, solar irradiance, and ENSO (Fig. 1). There was a high correlation ($r = 0.94$, 1951-2018) between the modeled ΔT (total sum of individual factors) and the observed ΔT , indicating that most of the perturbation in the observed ΔT was captured in our study.

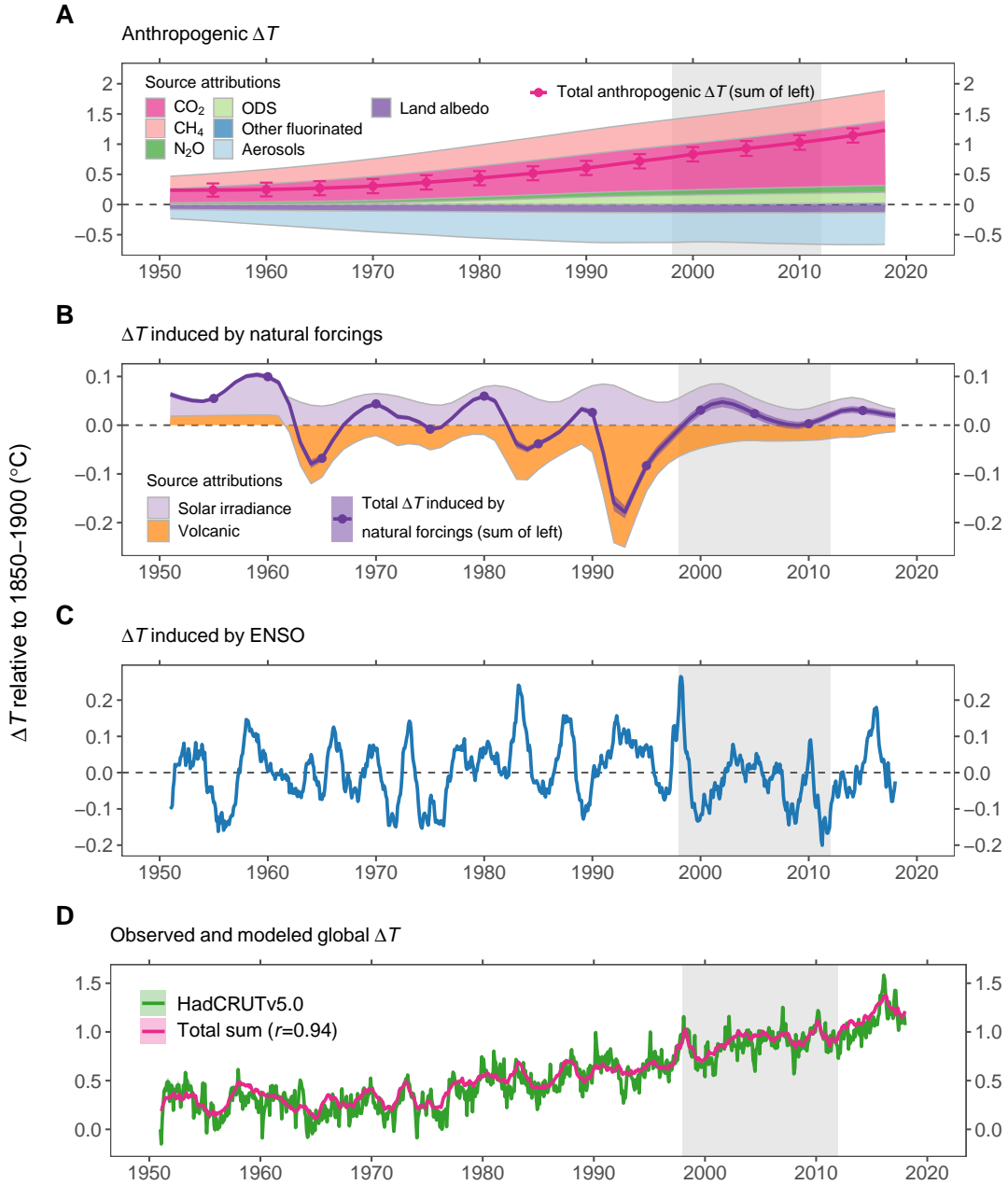


Figure 1: Anthropogenic and natural ΔT . (A) Anthropogenic ΔT . The thick red solid line and error bars indicate total anthropogenic ΔT . (B) ΔT caused by natural forcings. The thick purple solid line and range represent the total ΔT induced by natural forcings. Color ribbons in (A and B) show ΔT caused by individual factors. (C) ΔT caused by ENSO. (D) HadCRUT5 and the total summed ΔT . Pearson's correlation between the total sum and HadCRUT5 is shown in (D). The error bar in (A) and ranges in (B to D) are the one-sigma produced by the ensemble of statistical regressions. See materials and methods for further information on estimating uncertainty. The SW era from 1998 to 2012 is shaded in light gray.

Methane stabilization and ODS mitigation help slow global warming

Fig. 2A-L shows ΔT attributions by source, the total sum of all sources, and the observed ΔT HadCRUT5 to aid comparison. Gradients indicated by the thin solid and solid with extended dashed lines represent ΔT linear trends from 1951 to 2012 and from 1998 to 2012, respectively. Accordingly, to the left of the junction, if the dashed line is above the solid line, it implies that the growth rate is slowing, and vice versa. Methane, ODS, solar irradiance, and ENSO negatively contributed to ΔT during 1998-2012 compared to 1951-2012. The emission attributions of ΔT agree mostly with the AR6 forcing-based estimate (34) (fig. S2), except for halogenated ΔT , which is approximately twice as high as AR6. This is because our method generated a smaller negative ozone effective radiative forcing (ΔF) (-0.05 Wm^{-2} out of total ozone forcing 0.26 Wm^{-2} , 1850-2019), which was induced by halogenated gases (cf. -0.16 Wm^{-2} out of 0.47 Wm^{-2} , 1750-2019 (35), used in AR6) (see fig. S3 for the attribution of ozone effective ΔF). Consequently, a smaller ΔT was mitigated by ozone, and halogenated ΔT was positively larger in our results.

Based on the attributed ΔT , we computed the decadal trend (fig. S4) and DDT (Fig. 2M) for each source. Note that DDT was also affected by the referred historical period; selecting a smaller period of 1960-2012 would highlight such a slowdown more clearly because ΔT increased more rapidly throughout 1960-2012 (fig. S1). However, we examined 1951-2012 for a general case.

ENSO contributed the most to the SW, with a DDT of $-0.063 \pm 0.002 \text{ }^\circ\text{C/decade}$, followed by solar irradiance ($-0.033 \pm 0.002 \text{ }^\circ\text{C/decade}$). Anthropogenic ODS ($-0.016 \pm 0.007 \text{ }^\circ\text{C/decade}$) and methane ($-0.014 \pm 0.008 \text{ }^\circ\text{C/decade}$) also contributed to the SW. Specifically, ENSO and solar variations diminished warming directly with a negative decadal trend, while ODS and methane emissions simply exhibited a smaller decadal trend during 1998-2012 compared to that of 1951-2012. Other sources, including CO_2 , N_2O , other fluorinated gases, aerosols and

pollutants, land albedo, and volcanic activity, showed positive DDT, meaning that they increased faster between 1998 and 2012 than they did between 1951 and 2012. It is worth noting that the ΔT of total GHG emissions increased steadily (DDT 0.012 ± 0.015 °C/decade), masking the slowdown of ODS and methane ΔT (fig. S5), which is likely why previous research missed them. In addition, aerosols and pollutants and land albedo (see fig. S6 for the forcing trends) contributed to negative warming and declined over 1951-2012. However, during the SW period, their downward tendencies slowed and contributed to a positive DDT (see fig. S7).

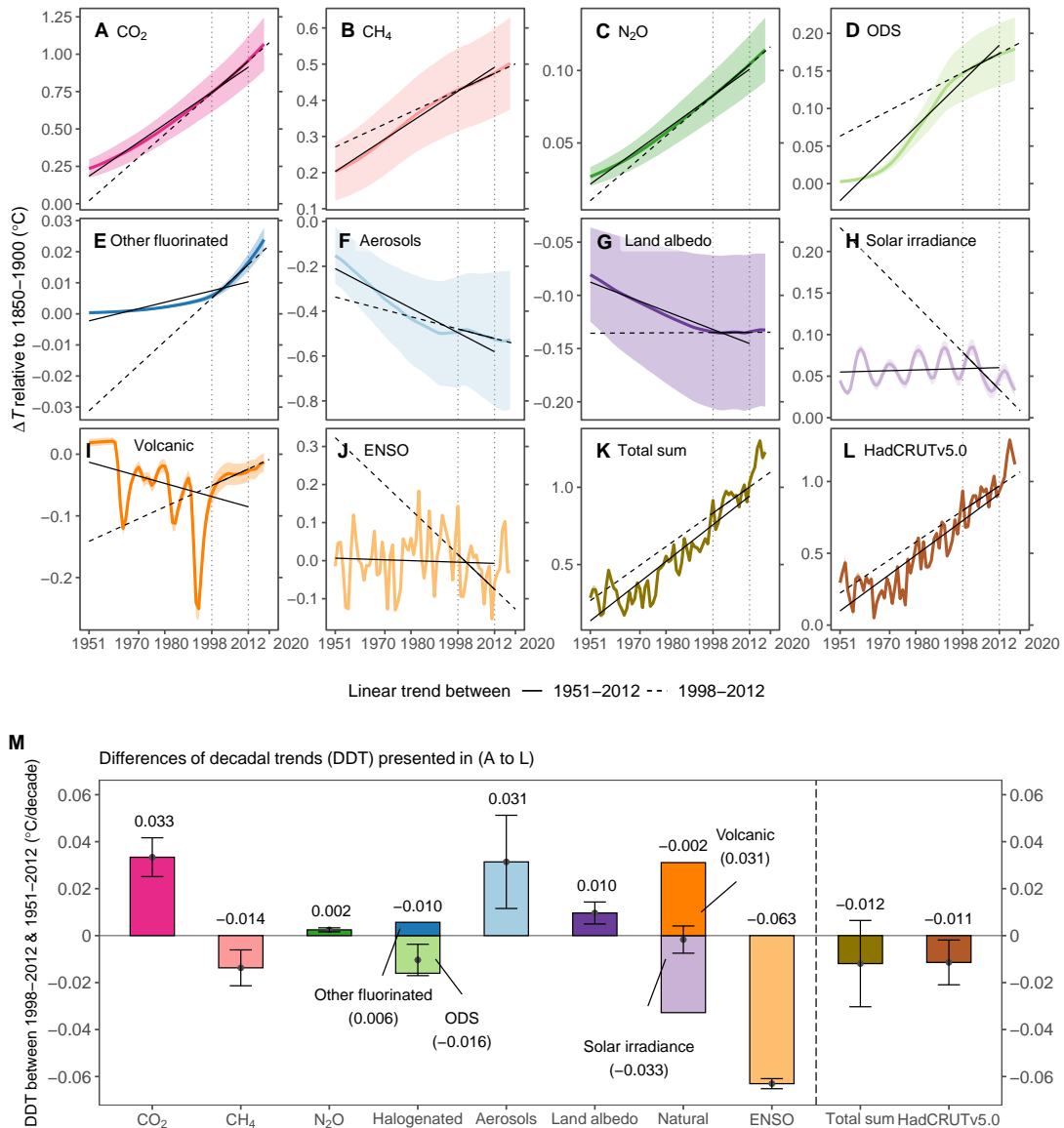


Figure 2: **Anthropogenic and natural ΔT by source and their DDT between 1998-2012 and 1951-2012.** (A to J) ΔT and uncertainty ranges caused by individual anthropogenic and natural factors. (K and L) The total sum and HadCRUT5 and their uncertainty ranges. Thin solid and solid with extended dashed lines denote linear trends from 1951 to 2012 and 1998 to 2012, respectively. (M) DDT derived from (A to L). The mean is displayed on top of the bar, and the error bar is the one-sigma produced by the ensemble of statistical regressions.

The slowdown of methane ΔT can be explained by the associated atmospheric concentrations (ΔC). Growths in methane ΔC is reported to have slowed from the 1980s and to have stabilized between 1999 and 2006 (36–41), owing in part to reductions in emissions from oil-gas exploitation and enteric fermentation in Europe and Russia (42). As shown in Fig. 3A, the DDT of methane ΔC simulated by SCM4OPT v3.3 presented a negative value of -52.4 ppb/decade, indicating that growths in methane ΔC slowed significantly during the SW period, which partly explains the slowdown of methane ΔT at the same time. Our results do not reflect methane emissions from natural sources, which accounted for approximately 39% of overall methane emissions in the recent decade (ref. (43), top-down estimate for 2008–2017). Furthermore, methane emissions from ultraemitters in the oil and gas industry, accounting for up to 12% of global methane emissions from oil and gas production and transmission (44), were not included in our calculations. Hence, the actual methane ΔC (for instance, DDT of CMIP6 ΔC -88.6 ppb/decade) may have contributed a more negative DDT in methane ΔT .

ODS manifested consistent DDT between the simulated ΔC (-224.9 CFC-12 equivalent ppt/decade) and the observed ΔC (CMIP6 -212.5 CFC-12 equivalent ppt/decade) (Fig. 3B) because they are well documented (40, 41, 45); hence, ΔC can be well captured by the model. ODS have been effectively mitigated under the Montreal Protocol since the late 1980s (46), resulting in a stabilized mixing ratio in the atmosphere. Such a tendency can also be used to interpret the negative DDT of ODS ΔT . The ΔC of other GHGs including CO₂, N₂O and other fluorinated gases, however, continued to rise, accelerating ΔT rather than slowing it during the SW era (fig. S8).

The emission-based attribution takes chemical-physical changes in the atmosphere into account. Methane ΔT , for example, includes ΔT produced by atmospheric methane ΔC , stratospheric water vapour from methane oxidation, the feedback on tropospheric ozone and on sinks of halogenated gases, and CO₂ from oxidized methane. Concerning ODS ΔT , their contribu-

tions contain ΔT caused by ODS ΔC and its feedback on stratospheric ozone and on methane sinks (Fig. 3B). A minor difference might exist between the ΔT resulting from ΔC and the associated emissions, but their major trends are consistent (Fig. 3, fig. S8). Therefore, the slowdown of ODS and methane ΔT during the SW can be robustly explained by their slowing trends in atmospheric ΔC . It is important to note that the slowing trends for both ΔC and ΔT induced by ODS and methane occurred earlier than 1998-2012, which also contributed to the SW.

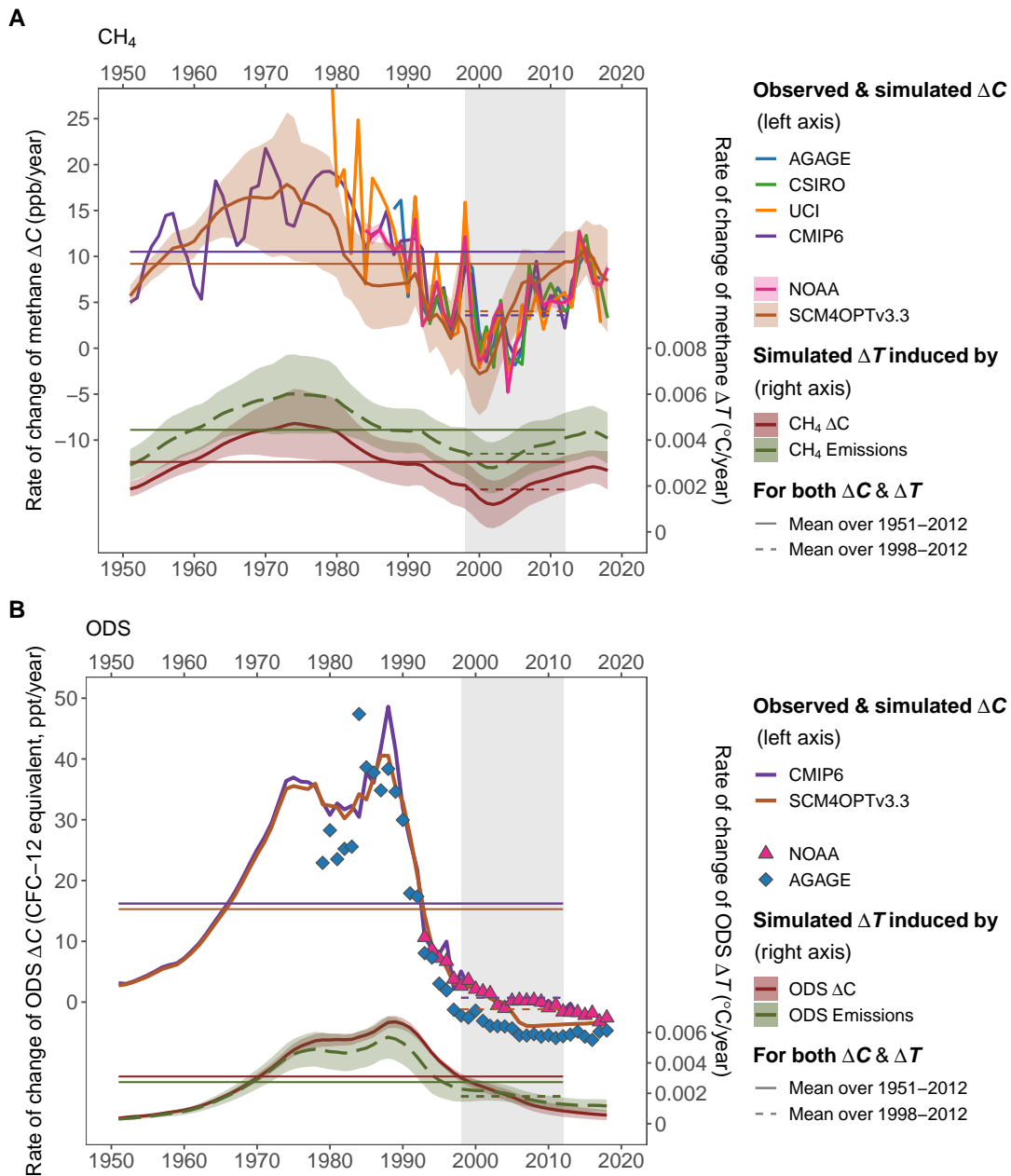


Figure 3: **Rate of change of methane and ODS ΔC and the induced ΔT .** (A) Methane and (B) ODS. The SCM4OPT v3.3 uncertainties in (A and B) are the one-sigma of the Monte Carlo simulation with $n = 1000$. ΔT uncertainty ranges in (A and B) are the one-sigma produced by the ensemble of statistical regressions. In (B), the ODS components for each source differ (table S2). Uncertainty is not considered in ODS ΔC because it is an equivalent value combining a collection of compounds of ODS (41). CMIP6 (41) and SCM4OPT v3.3 contain data for the entire evaluation period. Mean values from 1951 to 2012 and 1998 to 2012 are illustrated by thin horizontal solid and dashed lines, respectively. The SW era from 1998 to 2012 is shaded in light gray.

Contributions of natural forcing factors and ENSO

As shown in Fig. 4A, our natural forcing ΔT is in line with results from previous RCMs (47) as well as more complex Earth system models (ESMs) (48) (for GHGs and aerosols and pollutants, see figs. S5&S9). Fig. 4B depicts volcanic ΔF and ΔT . Although volcanic ΔF had a negative DDT ($-0.045 \text{ Wm}^{-2}/\text{decade}$), recovery from the cooling caused by large volcanic activities in the 20th century caused a long-term negative trend ($-0.012 \text{ }^\circ\text{C}/\text{decade}$, 1951-2012), whereas weak volcanic activity in the 1998-2012 period caused a small positive trend ($0.019 \text{ }^\circ\text{C}/\text{decade}$, 1998-2012), resulting in a positive DDT. In the case of solar irradiance (Fig. 4C), the decadal trends for both ΔF and ΔT became slower during 1998-2012 compared to 1951-2012. Thus, we can pin at least some of the cooling on the descending solar cycle. Regarding volcanic aerosols, in contrast to earlier studies (12, 14, 15), which could balance out up to 30% of anthropogenic ΔT (3), our results suggest that volcanic forcing is not responsible for the SW. Our result also implies a relatively large contribution from the descending solar cycle, similar to Lean (2018) (3), which mitigated approximately 36% of anthropogenic ΔT from 2001 to 2011. However, Lean (2018) also showed a small 8% cut in anthropogenic ΔT from volcanic aerosols at the same time, possibly due to the use of stratospheric aerosol optical depth (AOD) to estimate volcanic ΔT in her study, which is a proxy of volcanic aerosol ΔF . The volcanic ΔF actually presented a relatively small negative decadal trend ($-0.046 \text{ Wm}^{-2}/\text{decade}$, blue thin dashed line in Fig. 4B) from 1998-2012, which could produce the small volcanic cooling effect reported by Lean (2018).

ENSO was a major contributor to the SW, which was mainly led by strong La Niña cooling immediately after El Niño warming prior to 1998 (4, 5) (Fig. 4D). Because of its seasonality, ENSO contributed to SW in the form of an annual pulse signal (figs. S10-S13), whereas the descending solar cycle, ODS, and methane had a relatively continuous and stable influence on SW. Our result is consistent with that of Lean (2018), which signifies the largest contribution from

ENSO, with a cooling decadal trend of -0.086 °C/decade from 2001-2011 (cf. -0.065 °C/decade from 1998-2012 in this study, see fig. [S4](#)).

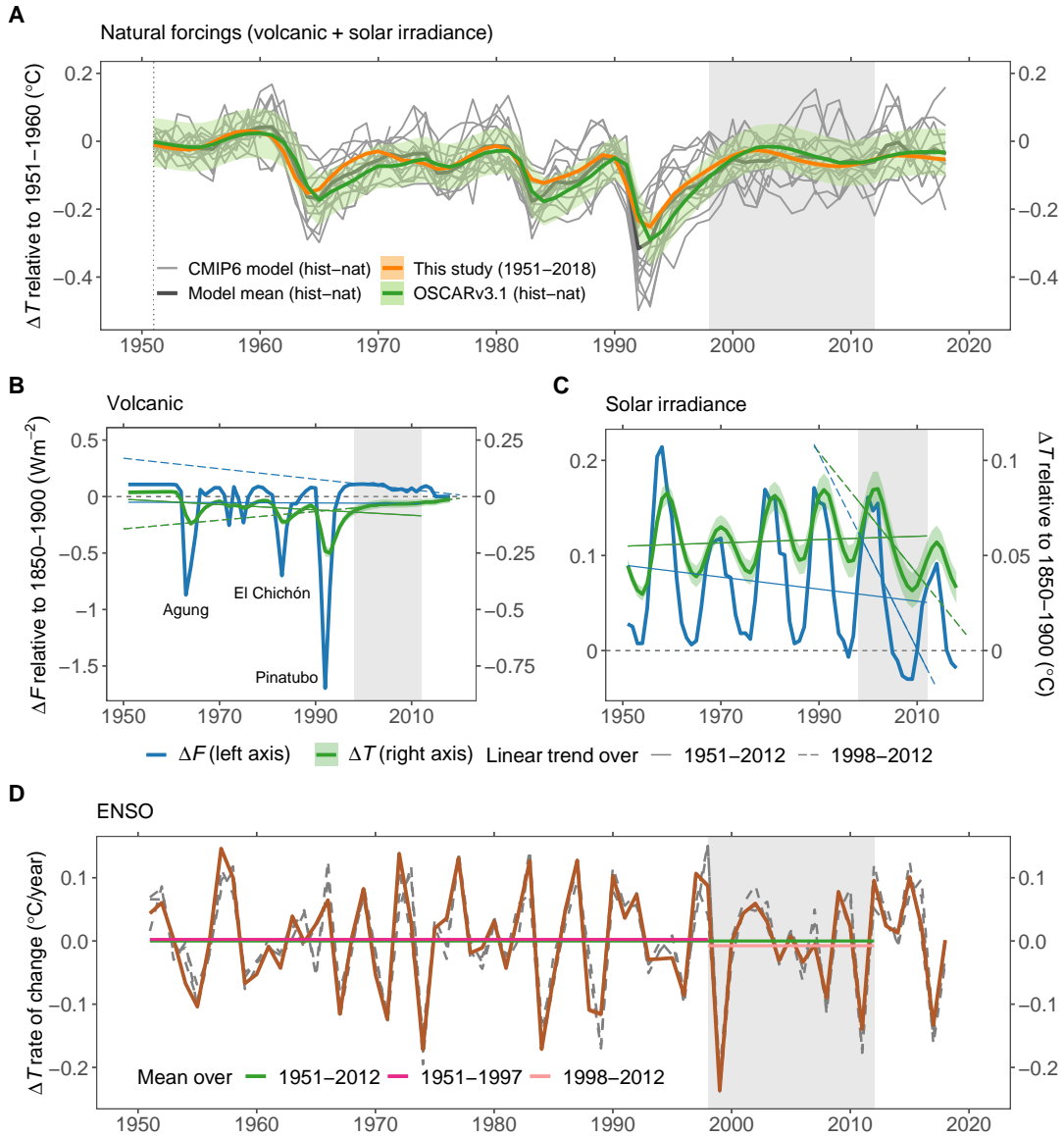


Figure 4: ΔT due to natural forces. (A) Natural forcing ΔT from OSCAR v3.1 (47) and CMIP6 Earth System Models (ESMs) (48) (ensemble mean for each ESM, table S3), as well as this study. OSCAR v3.1 uncertainty denotes the one-sigma obtained from Monte Carlo simulations with $n = 1000$. (B and C) ΔF and ΔT for volcanic eruptions and solar irradiance. In (B and C), thin solid and solid with extended dashed lines represent linear trends for the years 1951–2012 and 1998–2012, respectively. Three large volcanic eruptions are indicated in (B). (D) ΔT rate of change caused by ENSO (see fig. S10 for the ENSO ΔT trend). Gray dashed lines in (D) depict ΔT rates of changes estimated by using other ENSO indices shown in figs. S11–S13. Thick horizontal lines represent the mean values for the specified periods. The ΔT ranges of this study in (A to D) are the one-sigma produced by the ensemble of statistical regressions. The SW era from 1998 to 2012 is shaded in light gray.

Discussion and conclusions

The total sum of the DDT of individual factors converged on the observation (Fig. 2M), explaining almost all of the ΔT slowdown during the SW period. The use of different independent observations (figs. S14-S16) or ENSO indices (figs. S17-S19) gave similar results, implying that our analysis is quantitatively robust. The uncertainties may result from the autocorrelation of chosen predictors and cross-correlation among the predictors, as well as observational errors or inaccurate depictions of the real processes (3). The correlation between simulated ΔT and observed ΔT here is higher than Lean's (2018) statistical method ($r=0.91$ for space-based model during 1979–2017), most likely due to the full consideration of all available factors, which were derived from a physical RCM. This is also due to the use of the latest temperature record, while the older version may overmeasure the SW, resulting in larger residuals and lower goodness-of-fit (lower R-squared values) in the regression (fig. S20, table S4). Therefore, our causal explanation of the SW is sound.

Combining a physical RCM and an observationally constrained statistical model, we comprehensively evaluated the relative contributions to the SW from 1998-2012. Using DDT, we captured not only the direct cooling contributions but also the slowing trends of ΔT in the SW caused by anthropogenic and natural factors. Our results show that carbon dioxide, aerosols and pollutants and erupting volcanoes significantly accelerated global ΔT during the SW period compared to 1951-2012, whereas La Niña cooling and a descending solar cycle strongly offset the increased ΔT , accounting for approximately 50% and 26% of the total warming slowdown during 1998-2012 compared to 1951-2012. In particular, we identified that the reduced anthropogenic ODS and methane emissions also contributed approximately 13% and 11% of the total warming slowdown, which can be explained by the recorded atmospheric ΔC . Various factors superimposed on the timeline slowed ΔT between 1998 and 2012, while the beginning

and end of a single source did not necessarily match the SW period. The contribution of anthropogenic ODS and methane was comparable in scale to La Niña cooling and the descending solar cycle, as well as the overall downward trend exhibited by the temperature records (Fig. 2M), all of which can be detected with instruments, either directly or indirectly. Thus, our findings provide practical evidence for preventing global warming by reducing GHG emissions.

References

1. T. Stocker, *et al.*, *Technical Summary* (Cambridge University Press, Cambridge, United Kingdom and New York, NY, USA, 2013), book section TS, p. 33–115.
2. A. J. Simmons, *et al.*, *Quarterly Journal of the Royal Meteorological Society* **143**, 101 (2017).
3. J. L. Lean, *WIREs Climate Change* **9**, e511 (2018).
4. V. Eyring, *et al.*, *Human influence on the climate system* (Cambridge University Press, Cambridge, United Kingdom and New York, NY, USA, 2021), book section 3.
5. Y. Kosaka, S. P. Xie, *Nature* **501**, 403 (2013).
6. M. Watanabe, *et al.*, *Nature Climate Change* **4**, 893 (2014).
7. P. T. Brown, W. Li, S.-P. Xie, *Journal of Geophysical Research: Atmospheres* **120**, 480 (2015).
8. A. Dai, J. C. Fyfe, S.-P. Xie, X. Dai, *Nature Climate Change* **5**, 555 (2015).
9. B. A. Steinman, M. E. Mann, S. K. Miller, *Science* **347**, 988 (2015).
10. A. Pasini, U. Triacca, A. Attanasio, *Theoretical and Applied Climatology* **129**, 873 (2017).

11. J. L. Lean, D. H. Rind, *Geophysical Research Letters* **35** (2008).
12. S. Solomon, *et al.*, *Science* **333**, 866 (2011).
13. J. M. Haywood, A. Jones, G. S. Jones, *Atmospheric Science Letters* **15**, 92 (2014).
14. D. A. Ridley, *et al.*, *Geophysical Research Letters* **41**, 7763 (2014).
15. M. Huber, R. Knutti, *Nature Geoscience* **7**, 651 (2014).
16. B. D. Santer, *et al.*, *Nature Geoscience* **7**, 185 (2014).
17. C. Deser, R. Guo, F. Lehner, *Geophysical Research Letters* **44**, 7945 (2017).
18. C.-Y. Wang, S.-P. Xie, Y. Kosaka, Q. Liu, X.-T. Zheng, *Journal of Climate* **30**, 2679 (2017).
19. F. Estrada, P. Perron, B. Martínez-López, *Nature Geoscience* **6**, 1050 (2013).
20. Q.-B. Lu, *Atmosphere* **13** (2022).
21. S. Solomon, *et al.*, *Science* **327**, 1219 (2010).
22. G. A. Schmidt, D. T. Shindell, K. Tsigaridis, *Nature Geoscience* **7**, 158 (2014).
23. I. Medhaug, M. B. Stolpe, E. M. Fischer, R. Knutti, *Nature* **545**, 41 (2017).
24. C. Hedemann, T. Mauritsen, J. Jungclaus, J. Marotzke, *Nature Climate Change* **7**, 336 (2017).
25. S. Power, F. Delage, G. Wang, I. Smith, G. Kociuba, *Climate Dynamics* **49**, 53 (2017).
26. G. Foster, S. Rahmstorf, *Environmental Research Letters* **6**, 044022 (2011).
27. C. Trudinger, I. Enting, *Climatic Change* **68**, 67 (2005).

28. B. Li, *et al.*, *Nature* **531**, 357 (2016).
29. B. Fu, *et al.*, *Nature Climate Change* **10**, 851 (2020).
30. X. Su, *et al.*, *Earth's Future* **5**, 592 (2017).
31. X. Su, *et al.*, *Sustainability Science* **13**, 291 (2018).
32. Z. Nicholls, *et al.*, *Earth's Future* **9**, 1 (2021).
33. X. Su, K. Tachiiri, K. Tanaka, M. Watanabe, M. Kawamiya, *One Earth* **5**, 1 (2022).
34. IPCC, *Climate Change 2021: The Physical Science Basis. Contribution of Working Group I to the Sixth Assessment Report of the Intergovernmental Panel on Climate Change*, V. Masson-Delmotte, *et al.*, eds. (Cambridge University Press, Cambridge, UK and New York, NY, USA, 2021), book section SPM.
35. G. D. Thornhill, *et al.*, *Atmospheric Chemistry and Physics* **21**, 853 (2021).
36. E. G. Nisbet, E. J. Dlugokencky, P. Bousquet, *Science* **343**, 493 (2014).
37. E. G. Nisbet, *et al.*, *Global Biogeochemical Cycles* **30**, 1356 (2016).
38. M. Rigby, *et al.*, *Geophysical Research Letters* **35**, 2 (2008).
39. E. J. Dlugokencky, *et al.*, *Geophysical Research Letters* **36**, 3 (2009).
40. S. A. Montzka, E. J. Dlugokencky, J. H. Butler, *Nature* **476**, 43 (2011).
41. M. Meinshausen, *et al.*, *Geoscientific Model Development* **10**, 2057 (2017).
42. N. CHANDRA, *et al.*, *Journal of the Meteorological Society of Japan. Ser. II* **99**, 309 (2021).

43. M. Saunois, *et al.*, *Earth System Science Data* **12**, 1561 (2020).
44. T. Lauvaux, *et al.*, *Science* **375**, 557 (2022).
45. S. Montzka, *et al.*, *Chapter 1: Ozone-Depleting Substances (ODSs) and Related Chemicals* (World Meteorological Organization, 2011), pp. 1–108.
46. P. Forster, *et al.*, *Climate Change 2007: The Physical Science Basis. Contribution of Working Group I to the Fourth Assessment Report of the Intergovernmental Panel on Climate Change*, S. Solomon, *et al.*, eds. (Cambridge University Press, Cambridge, United Kingdom and New York, NY, USA, 2007), book section 2.
47. T. Gasser, *et al.*, *Biogeosciences* **17**, 4075 (2020).
48. N. P. Gillett, *et al.*, *Geoscientific Model Development* **9**, 3685 (2016).
49. J.-F. Lamarque, *et al.*, *Geoscientific Model Development* **6**, 179 (2013).
50. R. A. Houghton, *et al.*, *Biogeosciences* **9**, 5125 (2012).
51. E. Hansis, S. J. Davis, J. Pongratz, *Global Biogeochemical Cycles* **29**, 1230 (2015).
52. S. J. Smith, A. Rothwell, *Biogeosciences* **10**, 6323 (2013).
53. P. Friedlingstein, *et al.*, *Earth System Science Data* **12**, 3269 (2020).
54. K. Wolter, M. S. Timlin, *International Journal of Climatology* **31**, 1074 (2011).
55. C. A. Smith, P. D. Sardeshmukh, *International Journal of Climatology* **20**, 1543 (2000).
56. M. Etminan, G. Myhre, E. J. Highwood, K. P. Shine, *Geophysical Research Letters* **43**, 12,614 (2016).

57. G. Myhre, *et al.*, *Anthropogenic and Natural Radiative Forcing* (Cambridge University Press, Cambridge, United Kingdom and New York, NY, USA, 2013), book section 8, pp. 659–740.
58. B. Fu, *et al.*, *Proceedings of the National Academy of Sciences* **118** (2021).
59. O. Boucher, A. Borella, T. Gasser, D. Hauglustaine, *Atmospheric Environment* **267**, 118762 (2021).
60. D. W. J. Thompson, J. M. Wallace, P. D. Jones, J. J. Kennedy, *Journal of Climate* **22**, 6120 (2009).
61. R. M. Hoesly, *et al.*, *Geoscientific Model Development* **11**, 369 (2018).
62. M. Crippa, *et al.*, GHG emissions of all world: 2021 report, *Tech. rep.* (2021).
63. M. Crippa, *et al.*, CO₂ emissions of all world countries – JRC/IEA/PBL 2022 Report, *Tech. rep.* (2022).
64. IPCC, *Climate Change 2021: The Physical Science Basis. Contribution of Working Group I to the Sixth Assessment Report of the Intergovernmental Panel on Climate Change*, V. Masson-Delmotte, *et al.*, eds. (Cambridge University Press, Cambridge, UK and New York, NY, USA, 2021), book section Annex III.

Acknowledgments

The computational resources were provided by the National Institute for Environmental Studies (NIES), Japan. **Funding:** This work was supported by the Decarbonized and Sustainable Society Research Program at the National Institute for Environmental Studies, Japan, and the

Program for the advanced studies of climate change projection (SENTAN, Grant Number JP-MXD0722681344) from the Ministry of Education, Culture, Sports, Science and Technology (MEXT), Japan. K. Tanaka benefited from state assistance managed by the National Research Agency in France under the Programme d'Investissements d'Avenir under the reference ANR-19-MPGA-0008. **Author contributions:** X.S. designed the study, performed the simulations, produced all figures, and led the writing with contributions from all authors. H.S. provided insights to create the statistical model. **Competing interests:** The authors declare no competing interests. **Data and materials availability:** The data used in this analysis can be accessed online (last access for all, 22 May 2023): Coupled Model Intercomparison Project 6 (CMIP6) (<https://esgf-node.llnl.gov/projects/cmip6/>); Community Emissions Data System (CEDS) (<https://esgf-node.llnl.gov/search/input4mips/>); Emission Database for Global Atmospheric Research (EDGAR) v7.0 (Global Greenhouse Gas Emissions) (https://edgar.jrc.ec.europa.eu/dataset_ghg70); EDGAR v6.1 (Global Air Pollutant Emissions) (https://edgar.jrc.ec.europa.eu/dataset_ap61); Coupled Model Intercomparison Project Phase 6 (CMIP6) emissions from the Integrated Assessment Modeling Consortium (IAMC) (<https://esgf-node.llnl.gov/search/input4mips/>); The Atmospheric Chemistry and Climate Model Intercomparison Project (ACCMIP) (49) (<https://tntcat.iiasa.ac.at/RcpDb>); Carbon emissions from land use and land-cover change (50, 51) (<http://www.globalcarbonatlas.org/en/CO2-emissions>); Historical landcover change and wood harvest CO₂ emissions from the Max Planck Institute for Meteorology (MPI-M) (<https://www.mpimet.mpg.de/en/science/the-land-in-the-earth-system/working-groups/climate-biogeosphere-interaction/landuse-change-emission-data/>); Land-use change emissions from ref (52) (https://cdiac.ess-dive.lbl.gov/ftp/Smith_Rothwell_Land-Use_Change_Emissions/); Land-Use Harmonization (LUH2) (<https://luh.umd.edu/>); Historical greenhouse gas con-

centrations for climate modelling (CMIP6) (<https://doi.org/10.5194/gmd-10-2057-2017>); National Oceanic & Atmospheric Administration Carbon Cycle Greenhouse Gases (atmospheric concentrations of CO₂, CH₄ and N₂O) (<https://gml.noaa.gov/ccgg/>); The NOAA Ozone Depleting Gas Index (<https://gml.noaa.gov/odgi/>); Advanced Global Atmospheric Gases Experiment (AGAGE) (<https://agage.mit.edu/data/agage-data>); The Global Carbon Project (GCP) (53) (<https://www.globalcarbonproject.org>); Global Methane Budget (<https://www.globalcarbonproject.org/methanebudget/>); Hadley Centre/Climatic Research Unit Temperature (HadCRUT) v5.0 (<https://www.metoffice.gov.uk/hadobs/hadcrut5/>); Berkeley Earth (Global Temperature Data) (<https://berkeleyearth.org/data/>); NOAA GlobalTemp v5.1 (<https://www.ncei.noaa.gov/products/land-based-station/noaa-global-temp>); GISS Surface Temperature Analysis (GISTEMP v4) (<https://data.giss.nasa.gov/gistemp/>); NOAA MEI (54) (<https://psl.noaa.gov/enso/mei.old/mei.html>); MEI from NCEP-NCAR (<https://www.webberweather.com/multivariate-enso-index.html>); Cold Tongue Index (CTI) (<https://github.com/ToddMitchellGH/Cold-Tongue-Index>); “BEST” ENSO Index (55) (<https://psl.noaa.gov/people/cathy.smith/best/>). The code for reproducing the study will be deposited in the permanent repository Zenodo.

Supplementary Materials for

Anthropogenic contributions to slow warming over 1998-2012

Xuanming Su *et al.*

Corresponding author: Xuanming Su, su.xuanming@nies.go.jp

Materials and Methods

Figs. [S1](#) to [S22](#)

Tables [S1](#) to [S4](#)

References (56-64)

Materials and Methods

ΔT simulations

We used an RCM - SCM4OPT v3.3 (30–33) to simulate global ΔT trends resulting from anthropogenic factors (such as CO₂, CH₄, N₂O, halogenated gases (16 ODS and 23 other fluorinated gases), carbon monoxide (CO), nitrogen oxide (NO_x), volatile organic compounds (VOCs), sulfate (SO_x), black carbon (BC), organic carbon (OC), and land albedo) and natural forcings (such as volcanic and solar irradiance). SCM4OPT v3.3 was created by updating an older version, SCM4OPT v3.2 (33). We present a new parameterization for CH₄ forcing (56). The methane ΔT trend in this study was estimated using a hybrid of the new Etminan parameterization and a traditional technique as in AR5 (57), and the associated processes and parameters were used in the Monte Carlo simulation as below. The former showed a 25% higher CH₄ forcing than the latter (1750–2011), resulting in a lower DDT level of -0.015 ± 0.008 °C/decade (cf. -0.012 ± 0.007 °C/decade using AR5’s method) in the final attribution (figs. S21-S22).

A normalized marginal method (27, 28, 58, 59) was applied to SCM4OPT v3.3 for ΔT quantifications of climate forcers. ΔT trends induced by nonemission factors such as natural forcings including volcanoes and solar irradiance, as well as human factors such as land albedo resulting from land-use change, were quantified using a residual method: (1) one historical emulation with all emissions and nonemission factors as input; (2) one “exclusive” experiment for estimating land-use albedo ΔT trends with constant preindustrial land cover levels, and two “exclusive” experiments for estimating natural forcing ΔT trends by deleting volcanic or solar forcings from historical emulations. We compared ΔT obtained from historical and “exclusive” experiments, and the differences between the two experiments were ΔT trends caused by these nonemission factors. For the remaining ΔT , the normalized marginal method was used to quantify the emission-induced ΔT trends (33). We assumed that the ratio of a species’ (e) ΔT

to overall ΔT , defined as α_e^t , is proportional to the marginal effect of e divided by the total marginal effect. To estimate α_e^t , two simulations were carried out for each species: (1) one historical simulation as above and the resulting ΔT denoted as ΔT_{all} ; and (2) another identical simulation except emission e reduced by a fraction of $\epsilon = 0.001$ to calculate the ΔT termed as $\Delta T_{e,\epsilon}$. Therefore, the relative contribution α_e^t can be obtained:

$$\alpha_e^t = \frac{\Delta T_{all} - \Delta T_{e,\epsilon}}{\sum_{e'} (\Delta T_{all} - \Delta T_{e',\epsilon})} \quad (S1)$$

ΔT_e resulting from emission e can be calculated as follows:

$$\Delta T_e = \Delta T_{all} \cdot \alpha_e^t \quad (S2)$$

After calculating ΔT induced by emissions and nonemission factors, we classified the resulting ΔT as CO₂, CH₄, N₂O, ODS, other fluorinated gases, aerosols and pollutants, land albedo, volcanoes, and solar irradiance, considering their inherent characteristics and rates of change since the preindustrial revolution.

To estimate ΔT trends induced by GHGs ΔC (Fig. 3, fig. S8), we again used the above normalized marginal method for the forcing-driven mode of SCM4OPT v3.3. We calculated the associated ΔF from ΔC and applied $\epsilon = 0.001$ to ΔF to obtain the trend of ΔC -induced ΔT . The same β_{GHG} (as below) was multiplied to estimate the final ΔT induced by the GHG ΔC .

It is worth noting that the numbers of ODS or other fluorinated gases used in this study differ from the compiled data or observations (table S2). For example, a few ODS gases (such as CFC-13, CH₂Cl₂ and CHCl₃) and other fluorinated gases (such as SO₂F₂, C₇F₁₆, C₈F₁₈ and C₂Cl₄) were not included in our simulation due to data availability. However, the warming effects from these gases are relatively small, and our results retained almost the same total equivalent ΔC trends as the observations (Fig. 3, fig. S8). Therefore, our conclusions are unaffected.

Statistical model

ENSO has larger influences on the global ΔT than other internal variabilities (3, 11, 26, 60). We used ENSO to reflect the main changes due to internal variability. SCM4OPT v3.3 does not replicate ENSO. We employed a statistical model to correct the biases in the magnitude of the simulated ΔT , and distinguish ENSO influences from the observed ΔT (3, 11, 26). We hypothesized that the observed ΔT consists of ΔT induced by anthropogenic GHG emissions, other anthropogenic factors such as aerosols and pollutants and land albedo, natural forcings, and ENSO. Accordingly, the observed ΔT is defined as a multiple regression among the time series of these elements plus a residual component allowing for errors resulting from simulations and observations:

$$\begin{aligned}
 \Delta T_{obs}(t) = & \beta_{GHG}(\Delta T_{CO_2}(t) + \Delta T_{CH_4}(t) + \Delta T_{N_2O}(t) + \Delta T_{ODS}(t) + \Delta T_{oFGS}(t)) \\
 & + \beta_{non-GHG}(\Delta T_{aero}(t) + \Delta T_{lcc}(t)) \\
 & + \beta_{nat}(\Delta T_{volc}(t) + \Delta T_{solar}(t)) \\
 & + \beta_{MEI}^1 MEI(t - \tau_1) + \beta_{MEI}^2 MEI(t - \tau_2) + \beta_{MEI}^3 MEI(t - \tau_3) \\
 & + Resi(t) \\
 & + T_0
 \end{aligned} \tag{S3}$$

where $\Delta T_{obs}(t)$ is the observed ΔT . $\Delta T_{CO_2}(t)$, $\Delta T_{CH_4}(t)$, $\Delta T_{N_2O}(t)$, $\Delta T_{ODS}(t)$, $\Delta T_{oFGS}(t)$, $\Delta T_{aero}(t)$, $\Delta T_{lcc}(t)$, $\Delta T_{volc}(t)$ and $\Delta T_{solar}(t)$ indicate the simulated ΔT caused by CO₂, CH₄, N₂O, ODS, other fluorinated gases, aerosols and pollutants, land albedo, volcanoes and solar irradiance, respectively. β_{GHG} , $\beta_{non-GHG}$ and β_{nat} are fitted coefficients for the associated factors. $MEI(t)$ indicates the monthly multivariate ENSO index (MEI) taken from existing literature (54). Before applying the MEI, we eliminated the linear trend from it. β_{MEI}^i and τ_i ($i = 1, 2, 3$) represent the fitted coefficients and the delayed months for the MEI, respec-

tively, which were selected to maximize the variance explained (table S4). $Resi(t)$ and T_0 are the residuals and intercept, respectively. The time series of the ΔT trends estimated from SCM4OPT v3.3 are bimonthly data, which we linearly interpolated into monthly values before employing in the statistical model. Multiple regression was applied to data from 1951 to 2018. The fitted coefficients, R^2 values and correlation coefficients are shown in table S4.

Uncertainties

This study considered uncertainties in historical emissions, climate model uncertainties, and uncertainties found in various observation records. First, three emission datasets, i.e., the Community Emissions Data System (CEDS) (61), Emission Database for Global Atmospheric Research (EDGAR) v7.0_GHG 1970-2021 and EDGAR v6.1_AP 1970-2018 (62, 63), and ACCMIP (49), were used to represent uncertainties resulting from estimates of historical emissions. We compiled and processed the data in the same way as ref. (33). When a certain species was not available, we used equivalent emission data from a separate dataset. These emissions were used to generate the atmospheric ΔC and the associated ΔF , and then to estimate the global ΔT . Second, we performed a Monte Carlo simulation with $n = 1000$ (see table S4 in the forcing study (33) for the parameter sets) for the climate system to calculate the climate model uncertainties. Third, we carried out regressions for individual temperature records or the representative record HadCRUT5 with different ENSO indices, considering that ENSO effects and residuals are somewhat sensitive to the temperature records and ENSO indices. The statistical regression was also performed using the Monte Carlo method with $n = 1000$. For example, the observed value was randomly chosen from the available dataset ensemble (for HadCRUT5 $n = 200$), while the predictor variables were randomly selected from the ensemble of SCM4OPTv3.3 simulations.

To estimate the uncertainty of aerosols presented in fig. S2, we summed the aerosols' ΔT

from AR6, namely, NO_x , VOC, SO_2 , OC, BC and NH_3 . Their uncertainties were propagated by assuming that the individual ΔT values are independent variables that are normally distributed. Thus, their sum was also normally distributed. For example, from $X \sim N(\mu_X, \sigma_X^2)$ and $Y \sim N(\mu_Y, \sigma_Y^2)$, we obtained the uncertainty of $Z = X + Y$: $Z \sim N(\mu_X + \mu_Y, \sigma_X^2 + \sigma_Y^2)$. A similar estimation was used in the AR6 calculation (https://github.com/sarambl/AR6_CH6_RCMIPFIGS).

Supplementary Figures

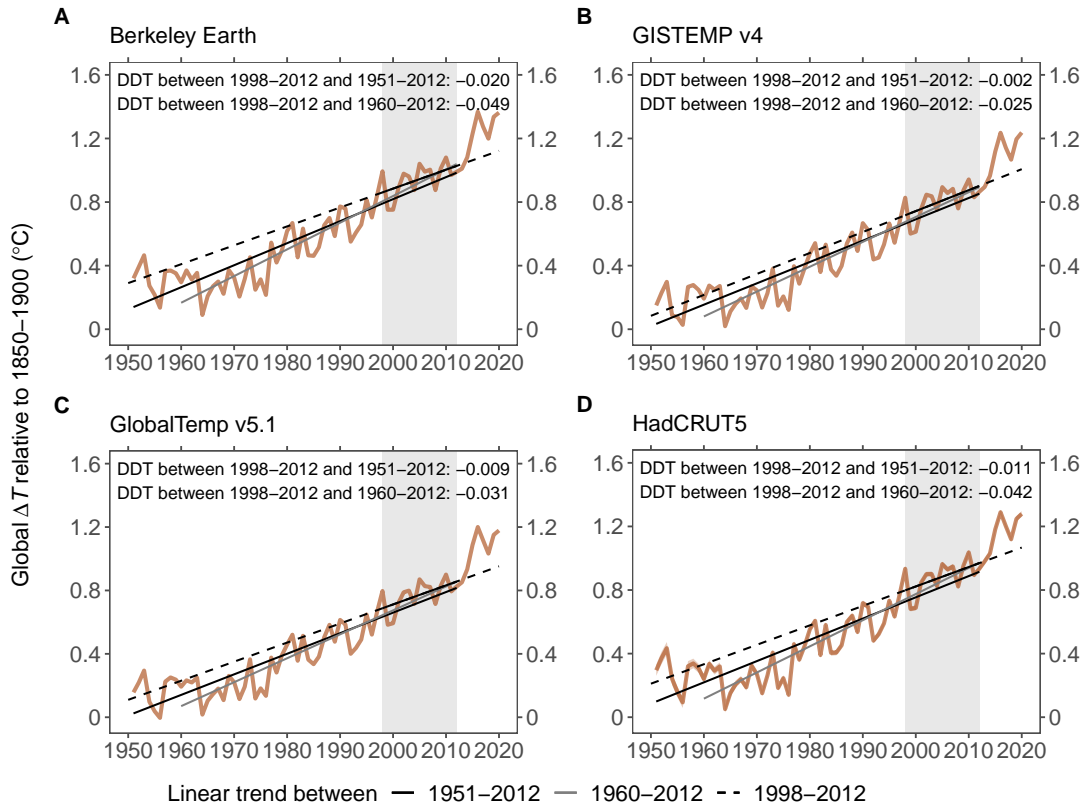


Figure S1: **Observed ΔT .** Linear trends across the selected periods are represented by solid and solid with extended dashed lines. ΔT of GISTEMPv4 is relative to 1880-1900 since there are no data available before 1880. Differences of decadal trends (DDT) are shown in the upper part of the panel for each temperature record. The SW era from 1998 to 2012 is shaded in light gray.

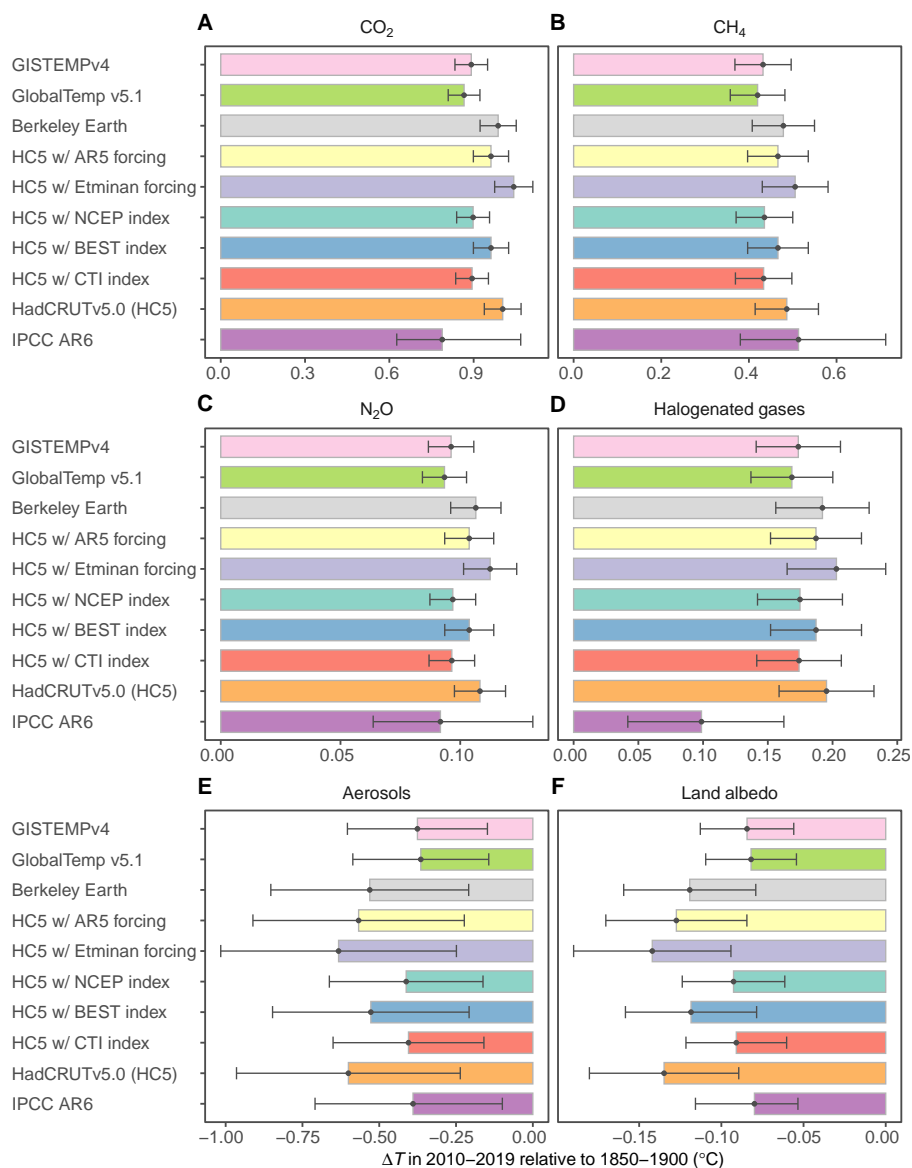


Figure S2: **Attributions of ΔT in this study vs. AR6.** The AR6 attribution was extracted from Figure SPM.2. Error bars in both this study and AR6 are one-sigma uncertainties. Note that Figure SPM.2 shows very likely ranges (5th-95th percentiles). We estimated the one-sigma uncertainty based on the AR6 calculation (https://github.com/sarambl/AR6_CH6_RCMIPFIGS) (see materials and methods).

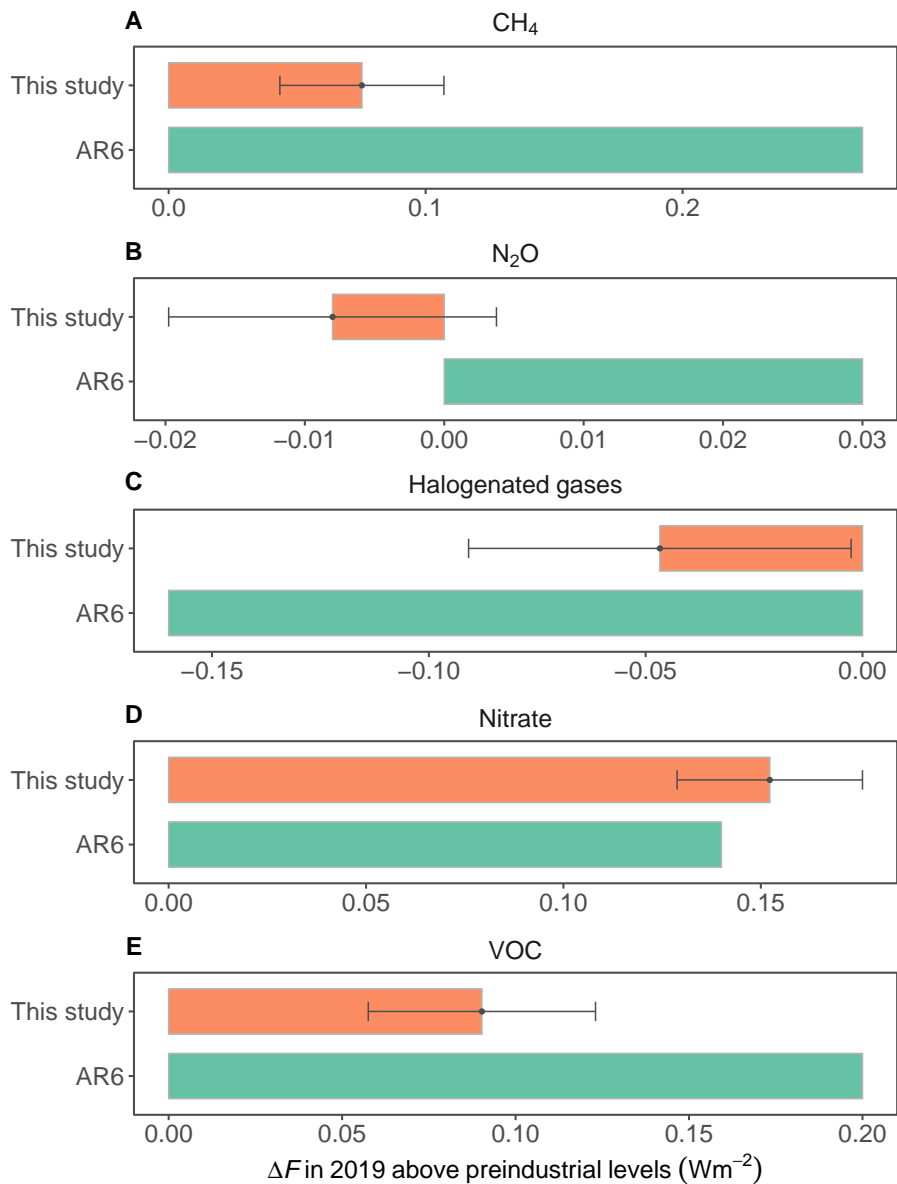


Figure S3: **Attribution of ozone effective ΔF in this study compared to AR6.** The effective ΔF for AR6 was extracted from https://github.com/sarambl/AR6_CH6_RCMIPFIGS. This study's evaluation period is 1850-2019, while AR6's evaluation period is 1750-2019. The effective ΔF for this study includes effects from both stratospheric and tropospheric ozone. This study's uncertainty ranges represent the one-sigma of the Monte Carlo simulation with $n = 1000$; however, the AR6 uncertainty ranges are not included due to data availability.

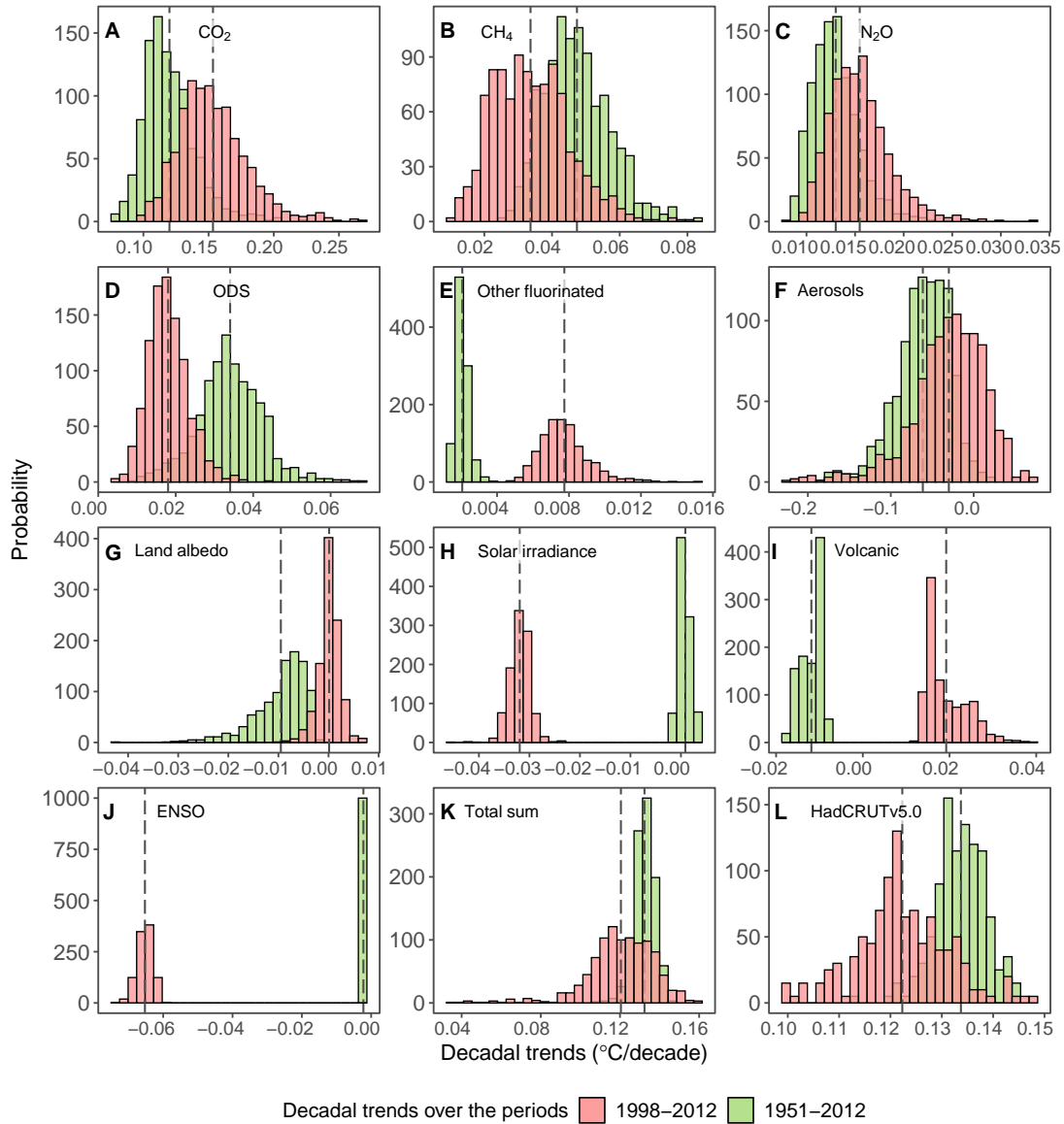


Figure S4: **Decadal ΔT trends.** The decadal ΔT trends are shown for the periods of 1998–2012 (red) and 1951–2012 (green). The histogram in (A to K) represents the distribution produced by the ensemble of statistical regressions, while the histogram in (L) shows the 200 realizations of the HadCRUT5 ensemble. The ensemble means are represented by vertical dashed lines over the selected periods. The ENSO is derived from HadCRUT5.

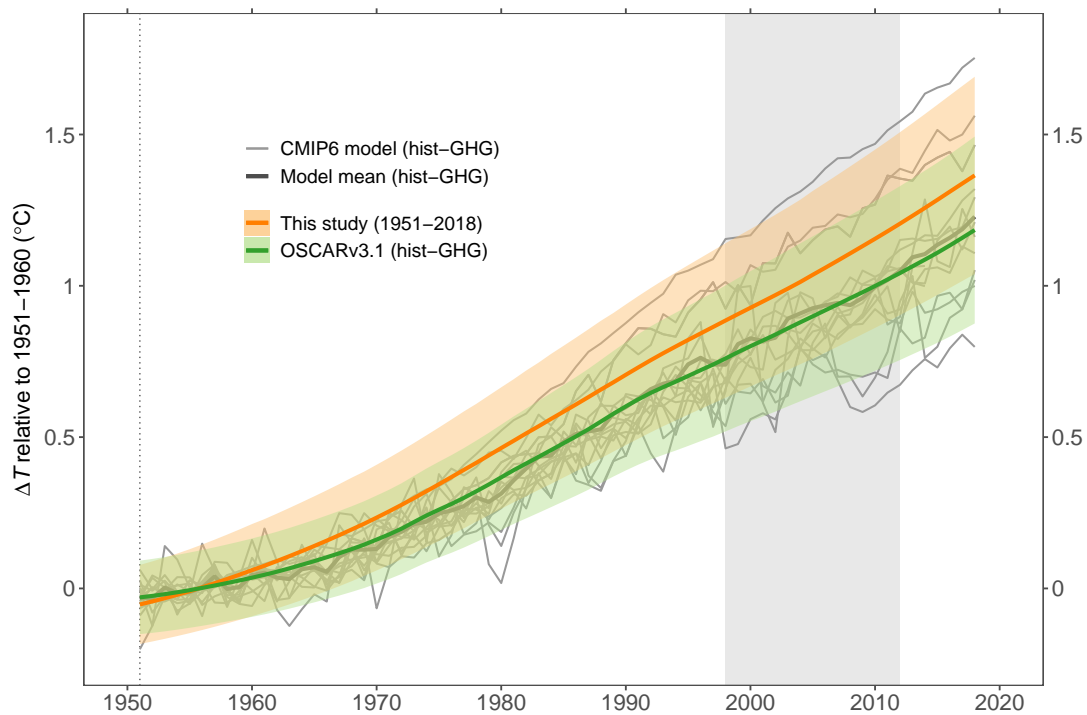


Figure S5: ΔT caused by GHG emissions. See Fig. 4 for the uncertainties of this study and OSCAR v3.1 (47). The SW era from 1998 to 2012 is shaded in light gray. Note that the hist-GHG simulation does not account for stratospheric and tropospheric ozone. See table S3 for the investigated CMIP6 ESMs (48).

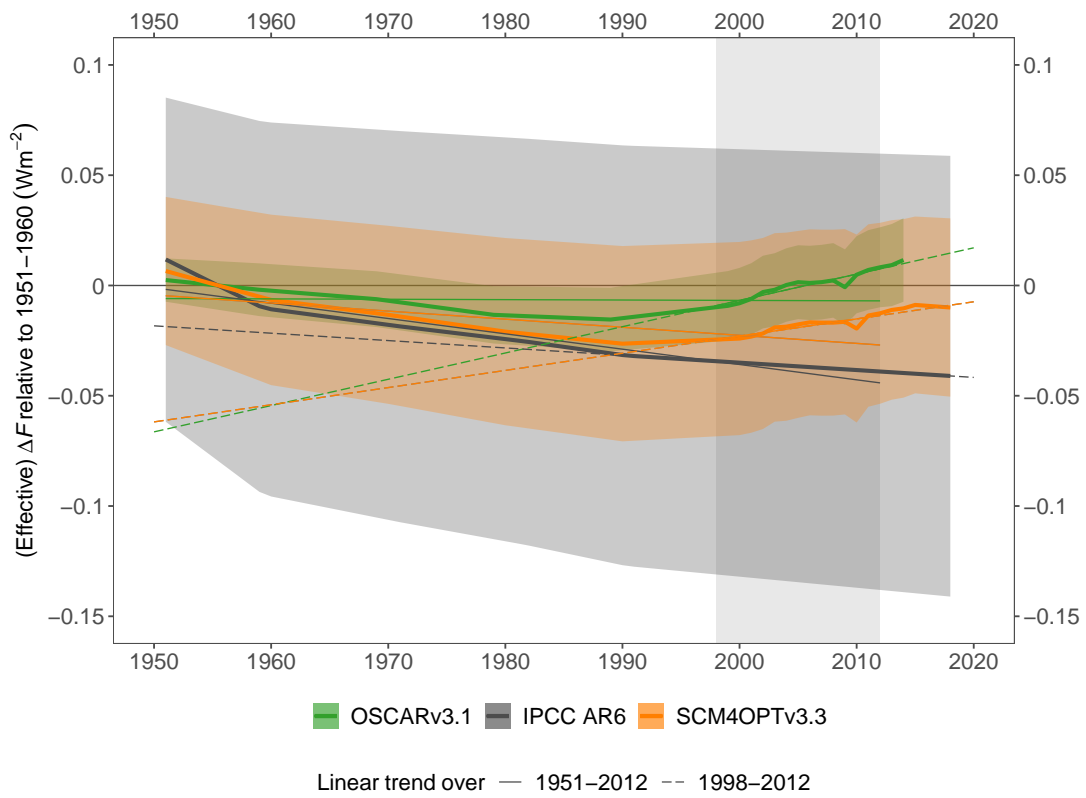


Figure S6: **(Effective) ΔF by anthropogenic surface albedo change.** IPCC AR6 (64) and SCM4OPT v3.3 are effective ΔF , whereas OSCARv3.1 (47) is ΔF due to data availability.

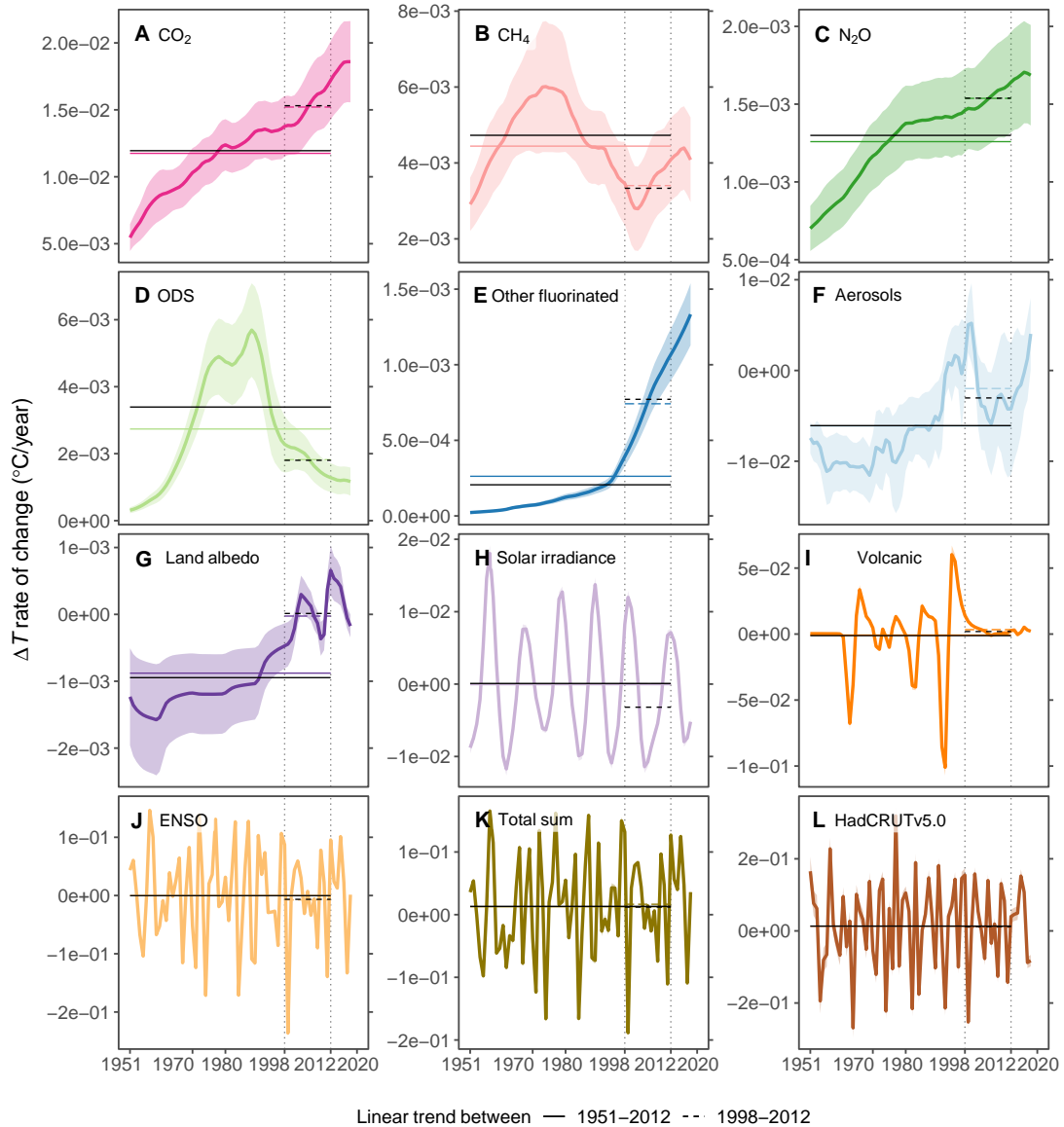


Figure S7: ΔT rate of change. Color horizontal solid and dashed lines represent mean values from 1951 to 2012 and from 1998 to 2012, respectively. Black horizontal solid and dashed lines represent the linear temperature trends from 1951 to 2012 and 1998 to 2012, respectively (Fig. 2 (A to L)). See Fig. 2 for the uncertainty description. HadCRUT5 was used to calculate the ENSO.

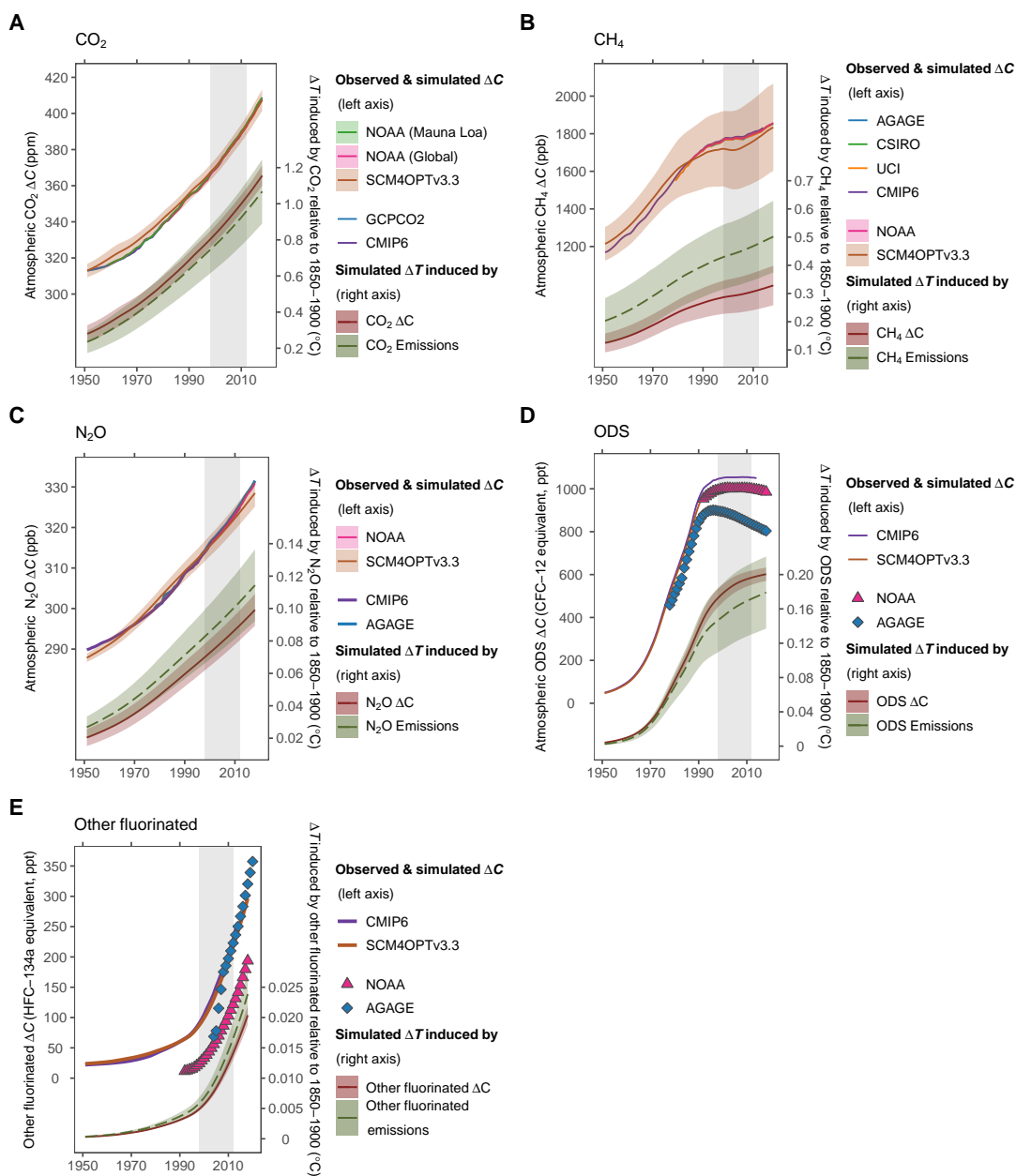


Figure S8: **Observed and simulated atmospheric ΔC and the induced ΔT .** See Fig. 3 for the uncertainty description. The components of ODS and other fluorinated gases for each source in (D and E) differ (table S2). Uncertainties are not considered in the ΔC of ODS and other fluorinated gases because they are equivalent values combining a collection of compounds (41). The SW era from 1998 to 2012 is shaded in light gray.

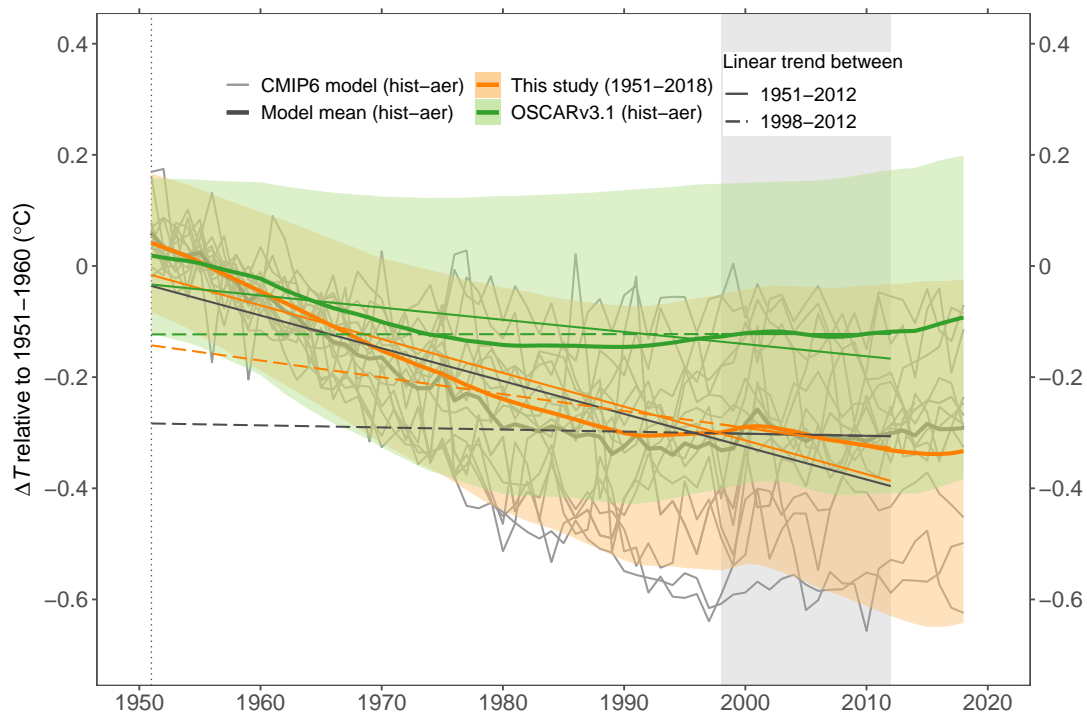


Figure S9: **Aerosol and pollutant-induced ΔT .** See Fig. 4 for the uncertainty description. The thin solid and solid with extended dashed lines represent linear trends for the years 1951-2012 and 1998-2012, respectively. The SW era from 1998 to 2012 is shaded in light gray. See table S3 for the investigated CMIP6 ESMs (48).

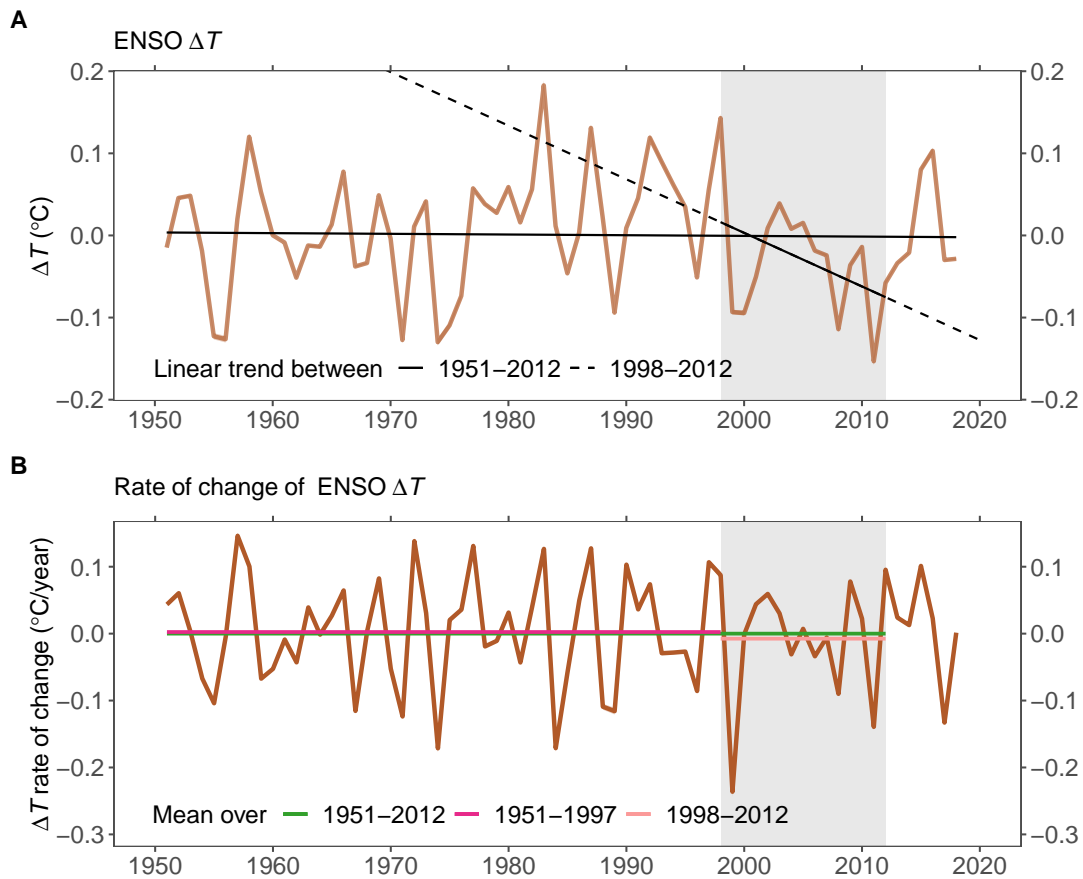


Figure S10: ΔT caused by ENSO. (A) ΔT trend caused by ENSO. Linear trends across the selected periods are represented by solid and solid with extended dashed lines. (B) Rate of change of ENSO ΔT . Thick horizontal lines represent the mean values for the specified periods. The MEI uses the NOAA MEI (54) (<https://psl.noaa.gov/enso/mei.old/mei.html>), which is the default MEI in this study. The ENSO is derived from HadCRUT5. The SW era from 1998 to 2012 is shaded in light gray.

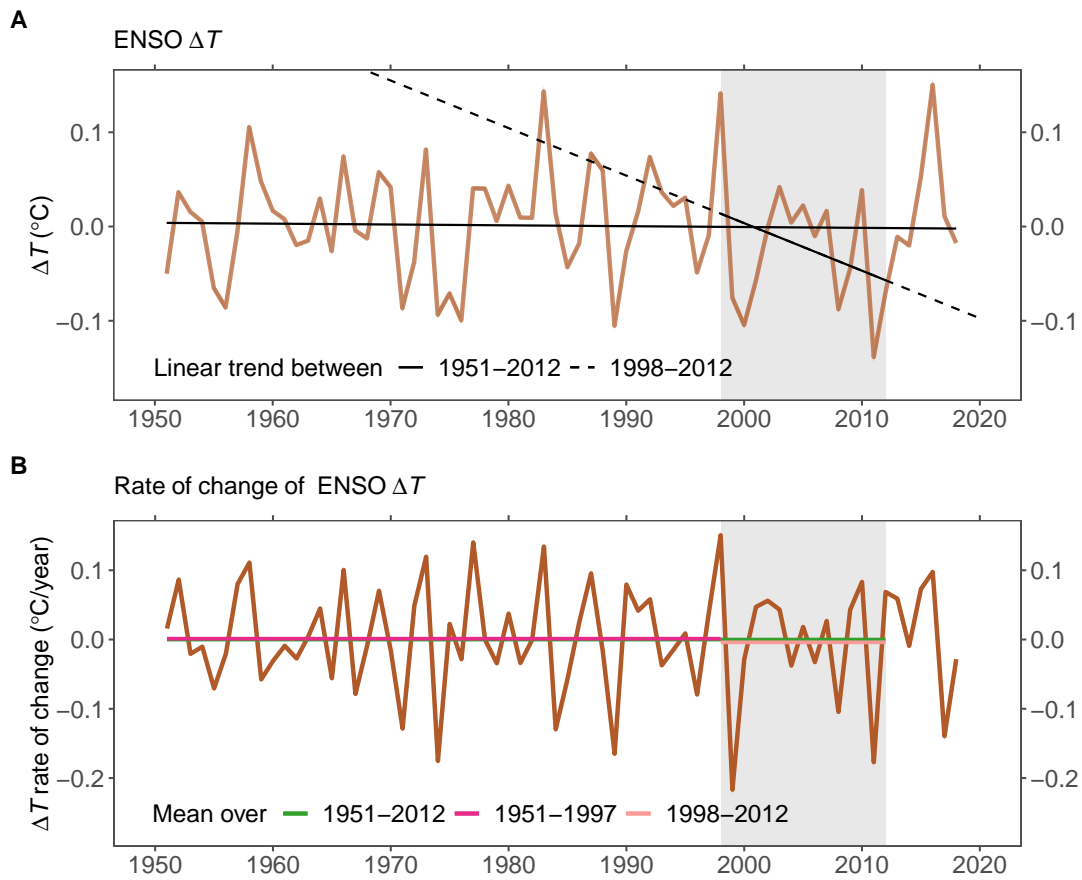


Figure S11: ΔT caused by ENSO. The same as in fig. S10, except that ENSO is estimated by using the MEI from NCEP-NCAR (<https://www.webberweather.com/multivariate-enso-index.html>).

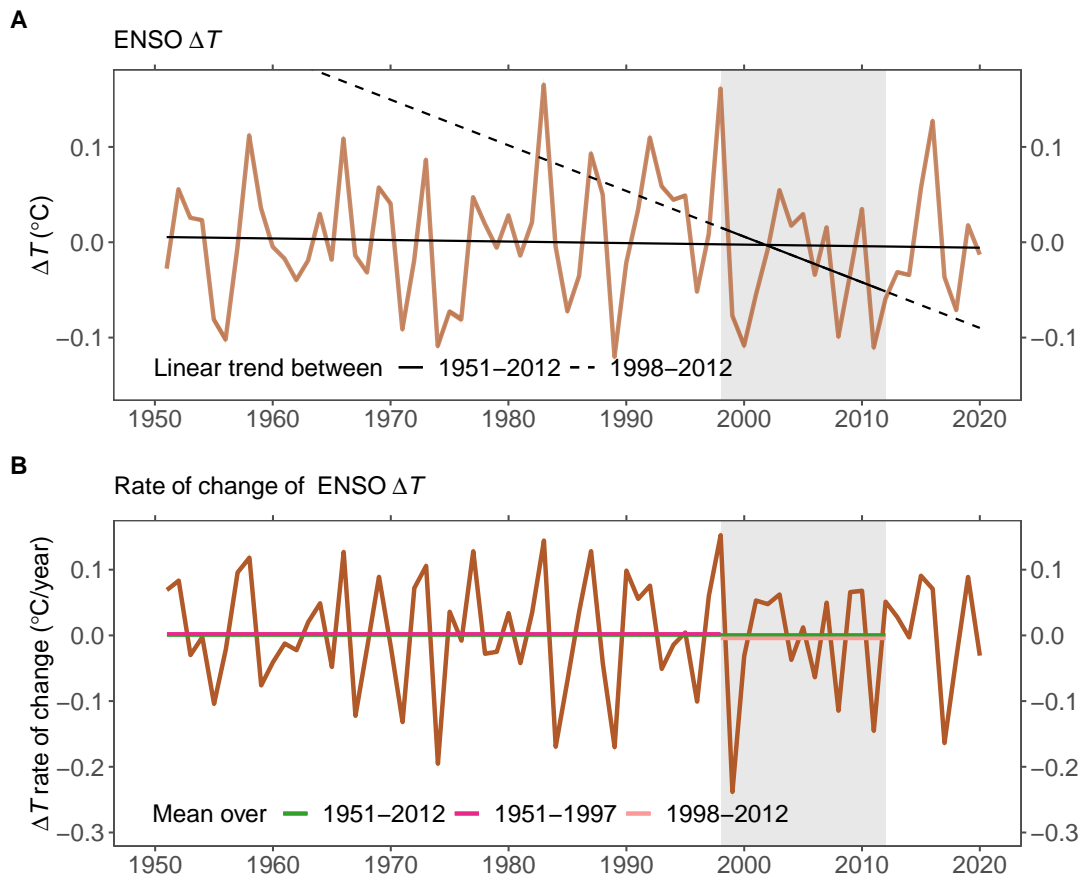


Figure S12: ΔT caused by ENSO. The same as in fig. S10, except that ENSO is estimated by using the cold tongue index (CTI) (<https://github.com/ToddMitchellGH/Cold-Tongue-Index>).

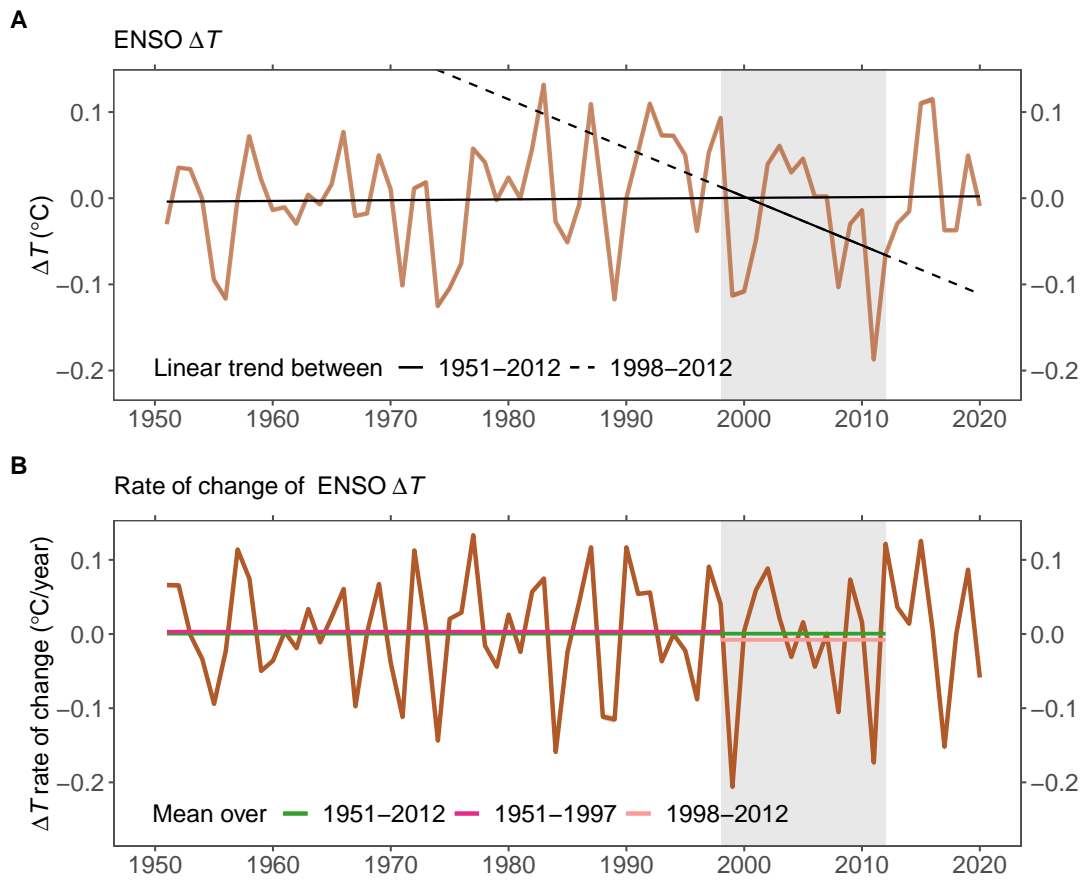


Figure S13: ΔT caused by ENSO. The same as in fig. S10, except that ENSO is estimated by using the “BEST” ENSO Index (55) (<https://psl.noaa.gov/people/cathy.smith/best/>).

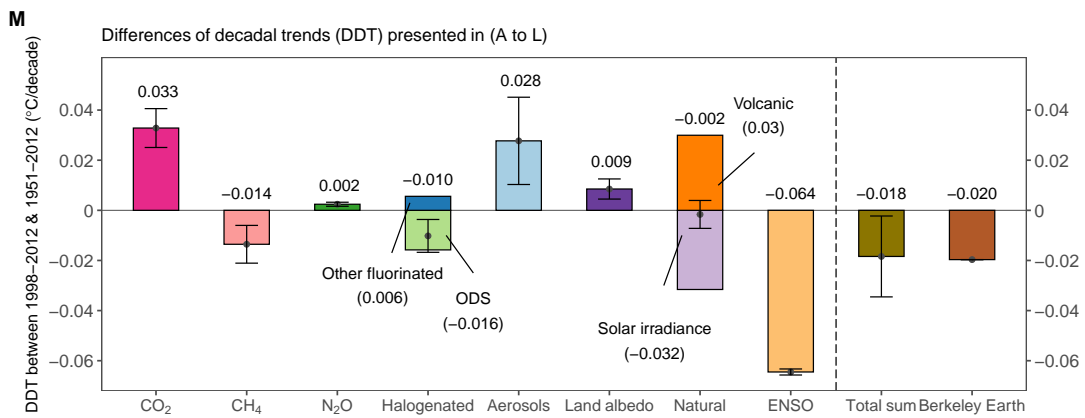
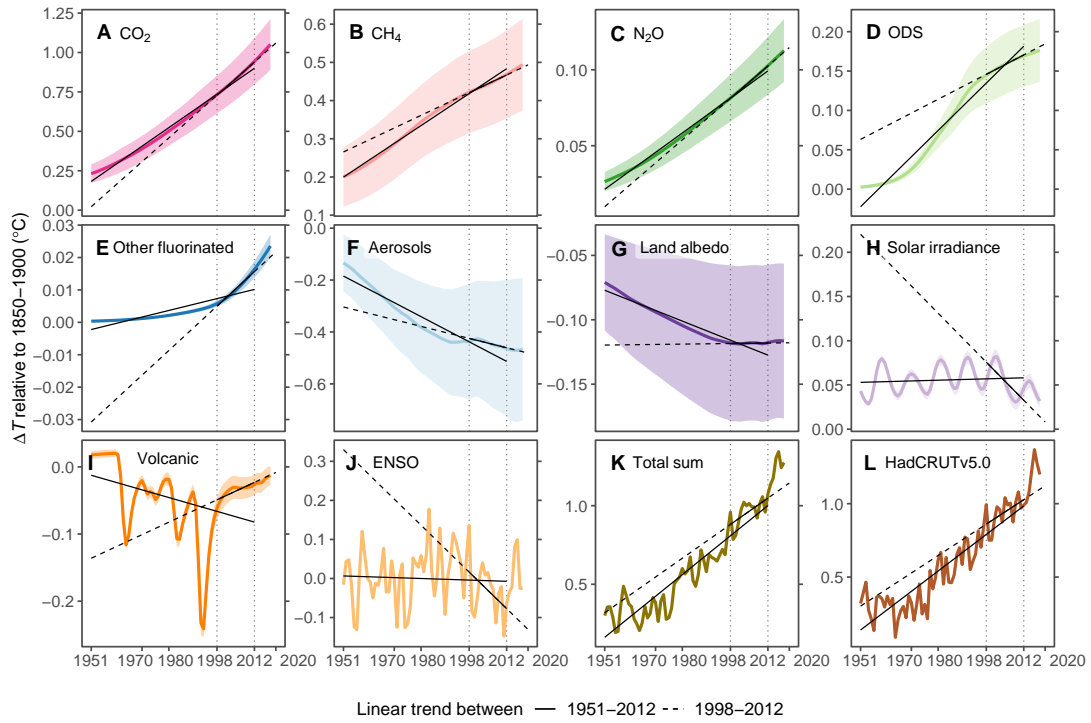


Figure S14: Anthropogenic and natural ΔT by source and their DDT between 1998-2012 and 1951-2012. The same as in Fig. 2, except that the temperature record uses Berkeley Earth.

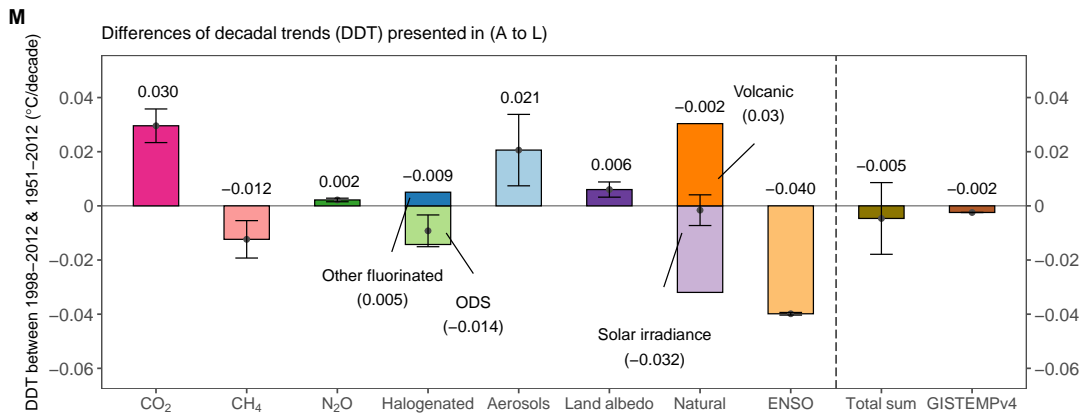
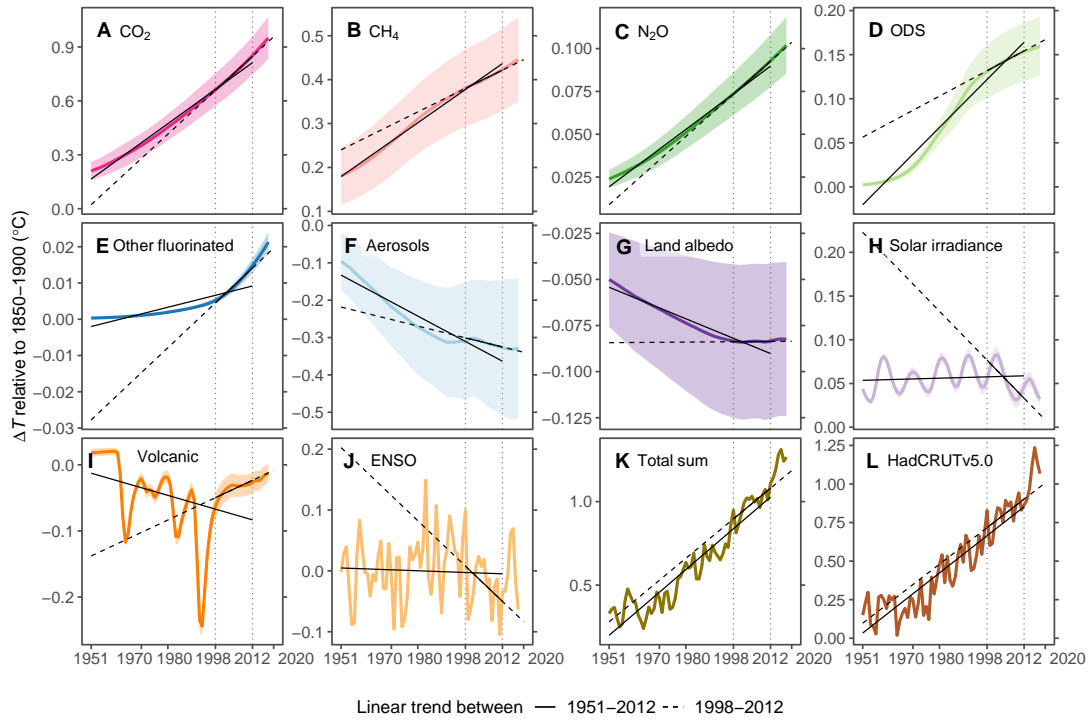


Figure S15: Anthropogenic and natural ΔT by source and their DDT between 1998-2012 and 1951-2012. The same as in Fig. 2, except that the temperature record uses GISTEMPv4.

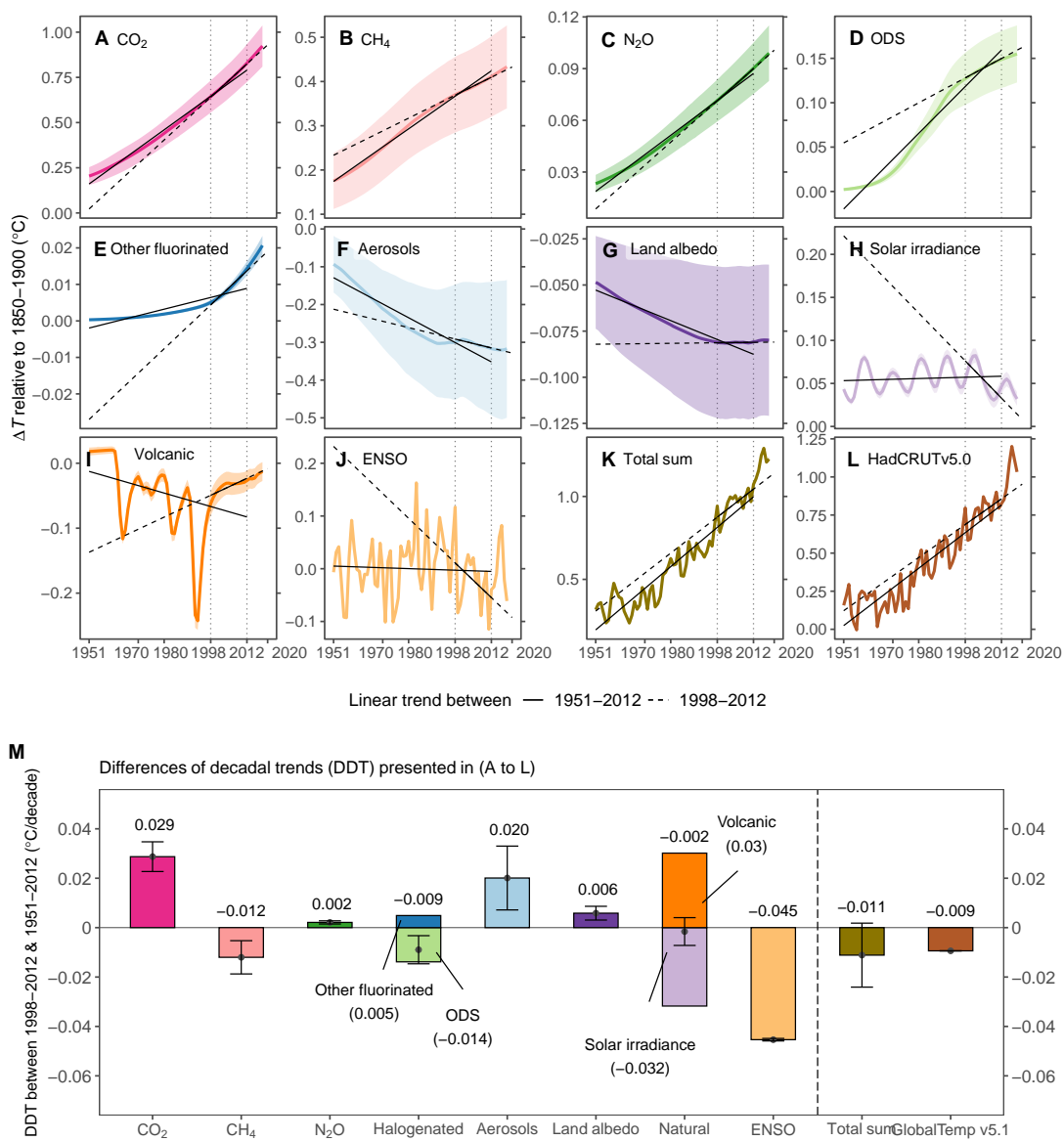


Figure S16: Anthropogenic and natural ΔT by source and their DDT between 1998-2012 and 1951-2012. The same as in Fig. 2, except that the temperature record uses GlobalTemp v5.1.

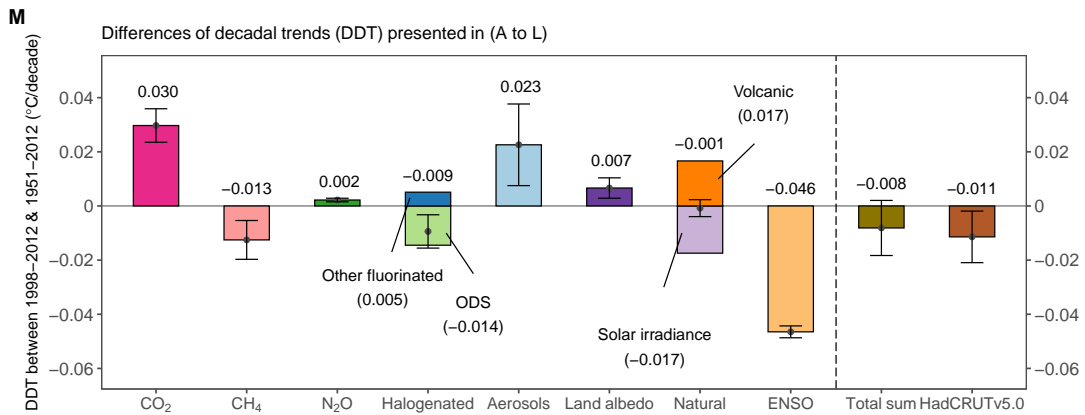
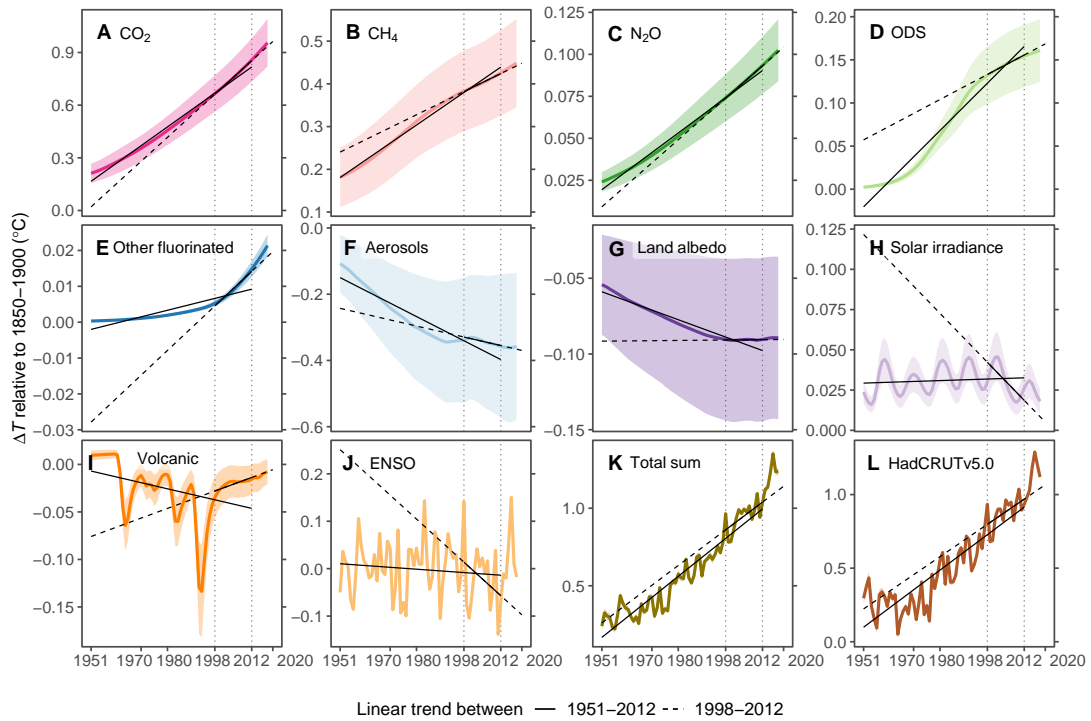


Figure S17: Anthropogenic and natural ΔT by source and their DDT between 1998-2012 and 1951-2012. The same as in Fig. 2, except that ENSO is estimated by using the MEI from NCEP-NCAR (<https://www.webberweather.com/multivariate-enso-index.html>).

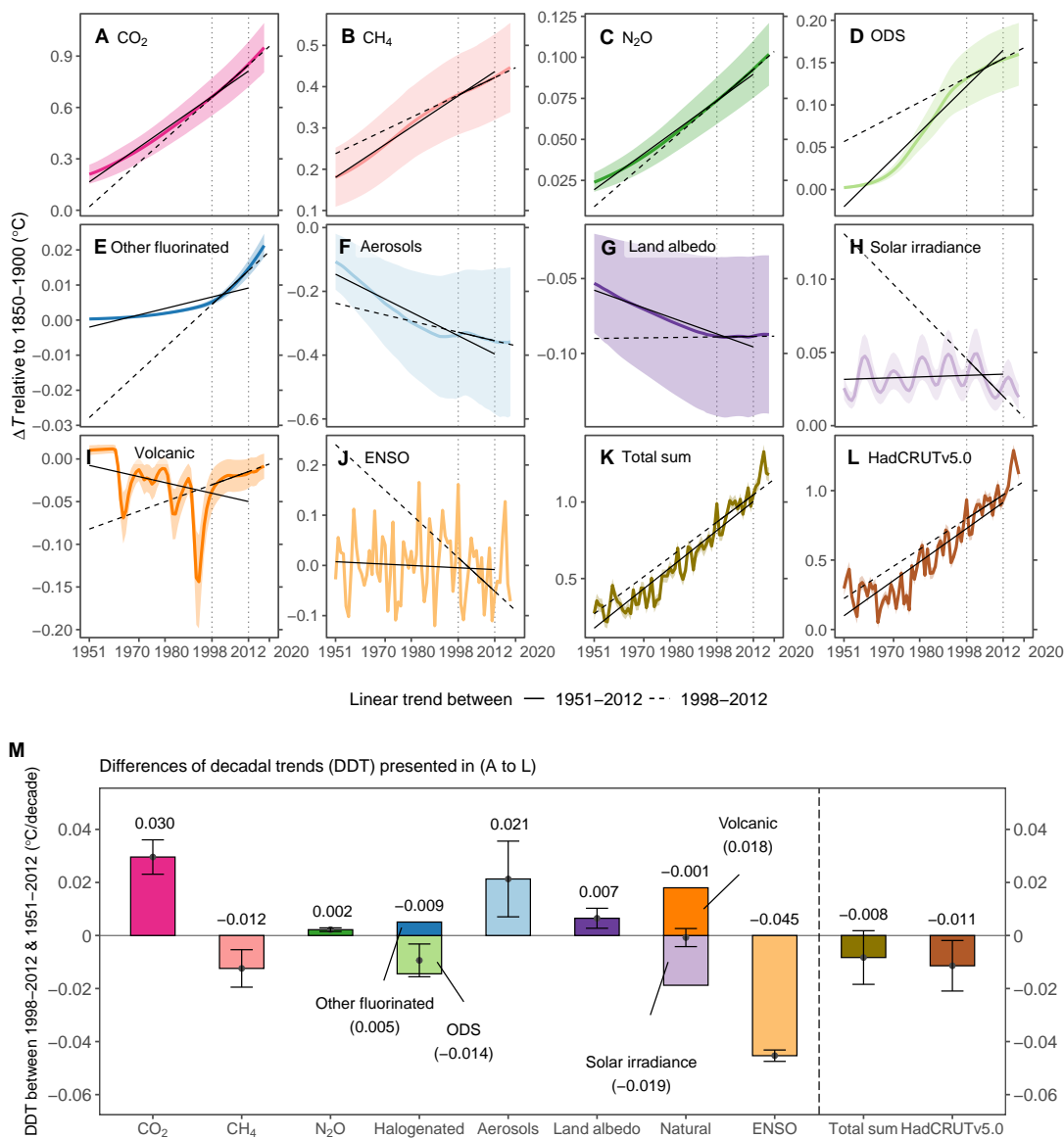


Figure S18: Anthropogenic and natural ΔT by source and their DDT between 1998-2012 and 1951-2012. The same as in Fig. 2, except that ENSO is estimated by using the cold tongue index (CTI) (<https://github.com/ToddMitchellGH/Cold-Tongue-Index>).

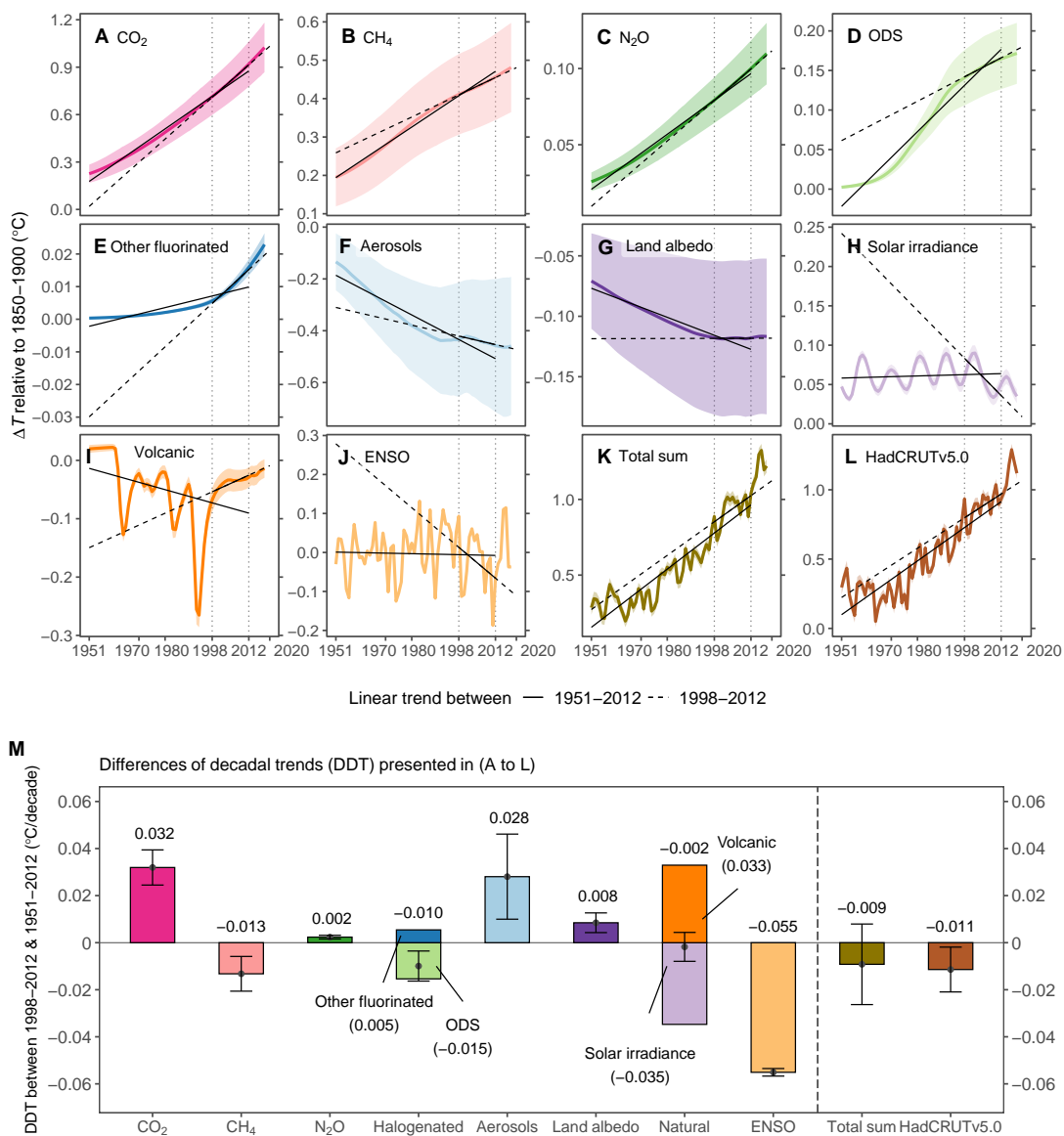


Figure S19: Anthropogenic and natural ΔT by source and their DDT between 1998-2012 and 1951-2012. The same as in Fig. 2, except that ENSO is estimated by using the “BEST” ENSO Index (55) (<https://psl.noaa.gov/people/cathy.smith/best/>).

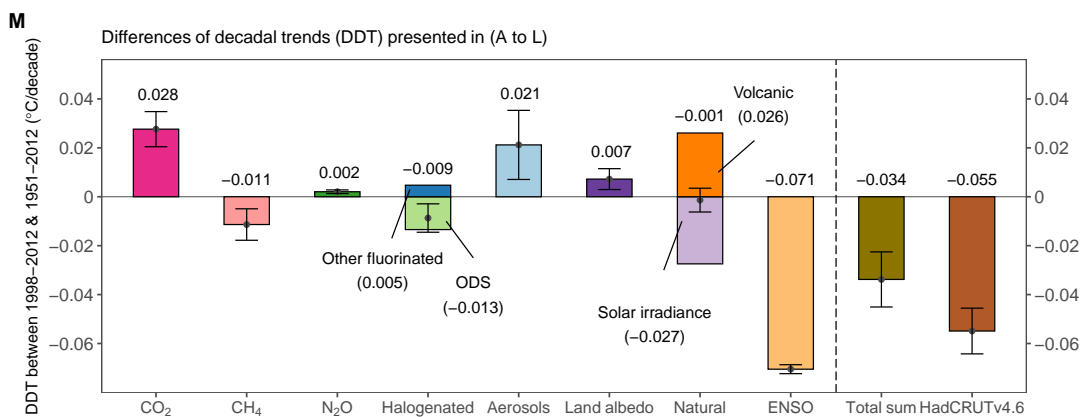
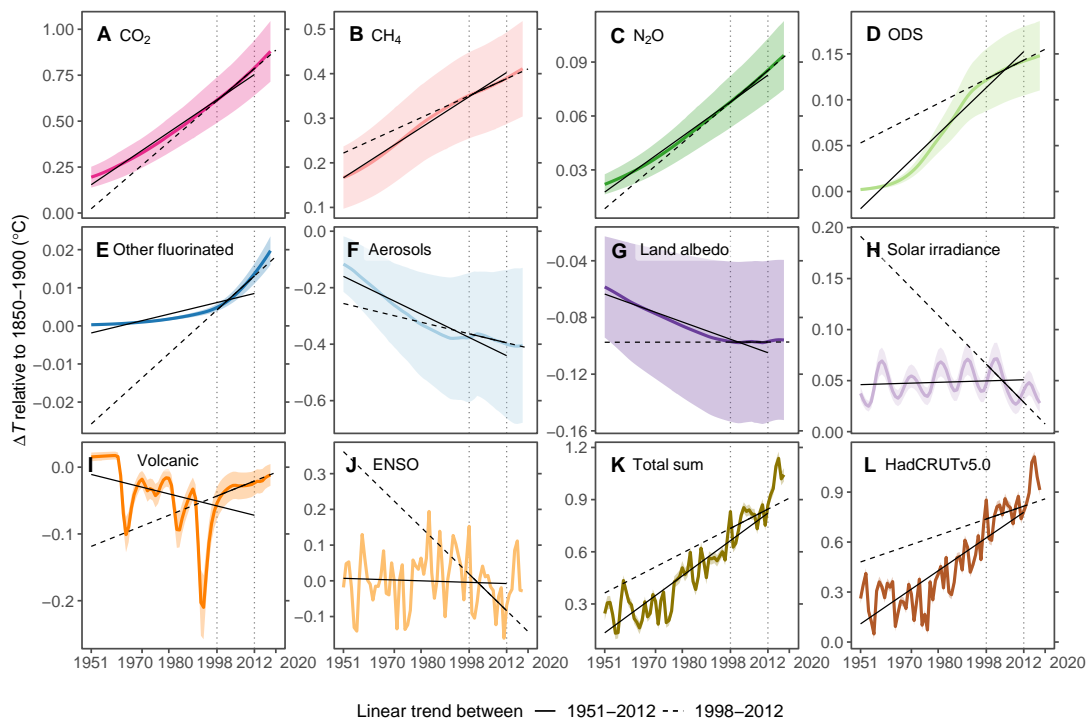


Figure S20: Anthropogenic and natural ΔT by source and their DDT between 1998-2012 and 1951-2012. The same as in Fig. 2, except that the temperature record uses HadCRUT4.6.

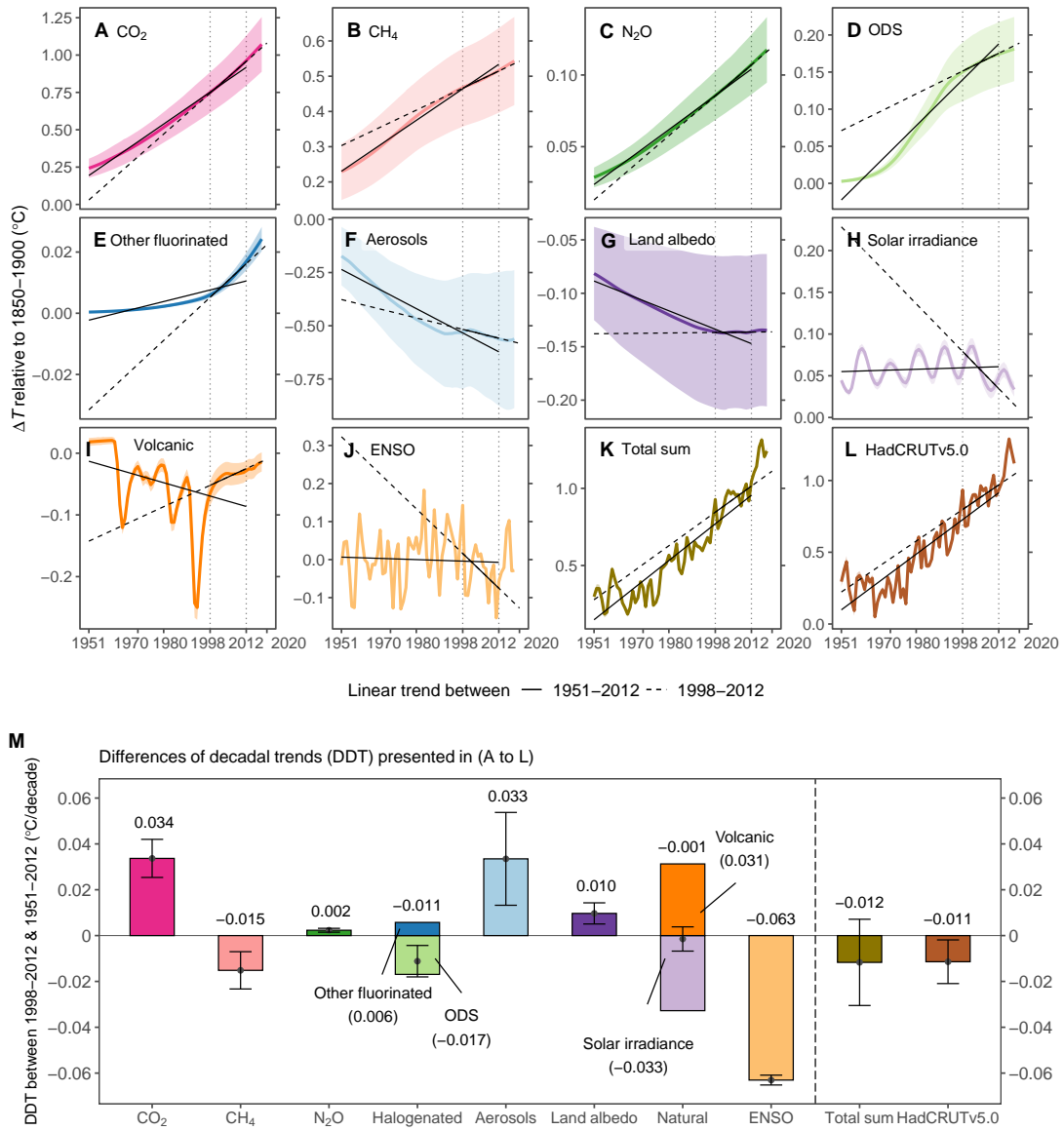


Figure S21: Anthropogenic and natural ΔT by source and their DDT between 1998-2012 and 1951-2012. The same as in Fig. 2, except that the methane forcing is parameterized using the Etminan method (56).

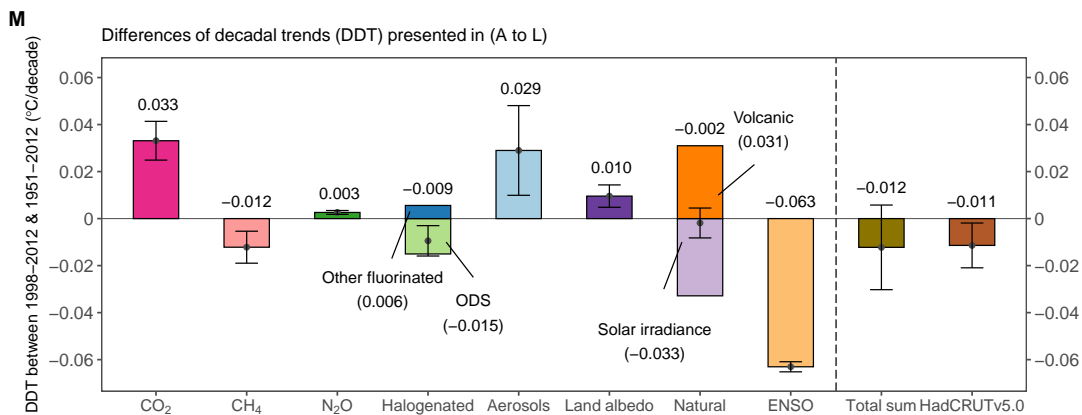
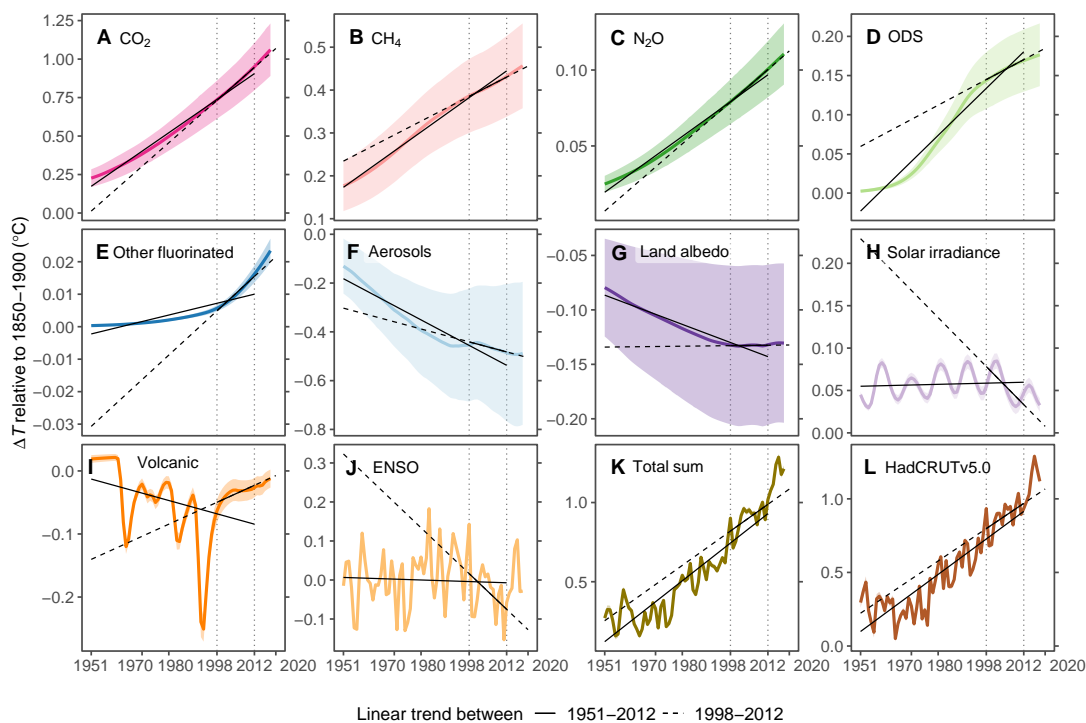


Figure S22: Anthropogenic and natural ΔT by source and their DDT between 1998-2012 and 1951-2012. The same as in Fig. 2, except that the methane forcing is parameterized using the usual IPCC method (57).

Supplementary Tables

Table S1: Test of statistical models using the Bayesian Information Criterion (BIC)

Index	Regression among variables	BIC	Remark
1	GHGs, Non-GHGs, natural, MEI	-1216.766	Used in this study
2	Total sum, MEI	-1180.292	
3	Anthropogenic, natural, MEI	-1205.087	
4	GHGs, aerosols, land albedo, natural, MEI	-1211.329	Negative coefficient occurs in land albedo, invalid
5	GHGs, Non-GHGs, volcanic, solar, MEI	-1216.033	
6	CO ₂ , CH ₄ , N ₂ O, ODS, other fluorinated, aerosols, land albedo, natural, MEI	-1206.71	Negative coefficients occur in CH ₄ , N ₂ O, other fluorinated and land albedo, invalid
7	CO ₂ , CH ₄ , N ₂ O, ODS, other fluorinated, aerosols, land albedo, volcanic, sola, MEI	-1225.454	Negative coefficients occur in CH ₄ , N ₂ O and land albedo, invalid

Table S2: List of halogenated compounds used in this study and observational records

Compounds	This study	CMIP6	NOAA	AGAGE.md (*)	AGAGE.ms (†)
Ozone-Depleting Substances (ODS)					
CFC-11	✓	✓	✓	✓	
CFC-12	✓	✓	✓	✓	
CFC-13					✓
CFC-113	✓	✓	✓	✓	✓
CFC-114	✓	✓			✓
CFC-115	✓	✓			✓
HCFC-22	✓	✓	✓		✓
HCFC-141b	✓	✓	✓		✓
HCFC-142b	✓	✓	✓		✓
CH ₃ CCl ₃	✓	✓	✓	✓	✓
CCl ₄	✓	✓	✓	✓	
CH ₃ Cl	✓	✓			✓
CH ₂ Cl ₂		✓			✓
CHCl ₃		✓		✓	✓
CH ₃ Br	✓	✓	✓		✓
Halon-1211	✓	✓	✓		✓
Halon-1202	✓				
Halon-1301	✓	✓	✓		✓
Halon-2402	✓	✓	✓		✓
Other fluorinated gases					
HFC-134	✓				
HFC-134a	✓	✓	✓		✓
HFC-23	✓	✓			✓
HFC-32	✓	✓	✓		✓
HFC-125	✓	✓	✓		✓
HFC-143	✓				
HFC-143a	✓	✓	✓		✓
HFC-152a	✓	✓	✓		✓
HFC-227ea	✓	✓	✓		✓
HFC-236fa	✓	✓			✓
HFC-245fa	✓	✓			✓
HFC-365mfc	✓	✓	✓		✓
HFC-41	✓				
HFC-43-10mcc	✓	✓			✓
NF ₃	✓	✓			✓
SF ₆	✓	✓			✓
SO ₂ F ₂		✓			✓
CF ₄	✓	✓			✓
C ₂ F ₆	✓	✓			✓
C ₃ F ₈	✓	✓			✓
C ₄ F ₁₀	✓	✓			
C ₅ F ₁₂	✓	✓			
C ₆ F ₁₄	✓	✓			
C ₇ F ₁₆		✓			
C ₈ F ₁₈		✓			
c-C ₄ F ₈	✓	✓			
C ₂ Cl ₄					✓

* AGAGE.md: AGAGE GC-MD data

(https://agage2.eas.gatech.edu/data_archive/global_mean/global_mean_md.txt)

† AGAGE.ms: AGAGE GCMS-Medusa data

(https://agage2.eas.gatech.edu/data_archive/global_mean/global_mean_ms.txt)

Table S3: The investigated CMIP6 ESMs and ensemble sizes

Index	Model	hist-GHG	hist-aer	hist-nat
1	ACCESS-CM2	3	3	3
2	ACCESS-ESM1-5	3	3	3
3	BCC-CSM2-MR	3	3	3
4	CanESM5	50	30	50
5	CESM2	3	2	3
6	CNRM-CM6-1	10	10	10
7	FGOALS-g3	3	3	3
8	GFDL-CM4	0	0	3
9	GFDL-ESM4	1	1	3
10	GISS-E2-1-G	10	15	20
11	HadGEM3-GC31-LL	5	5	10
12	IPSL-CM6A-LR	10	10	10
13	MIROC6	3	10	50
14	MRI-ESM2-0	5	5	5
15	NorESM2-LM	3	3	3

Table S4: Fitted coefficients for the statistical model

Corresponding figures and estimates	Berkeley Earth	GISTEMPv4	GlobalTemp v5.1	HadCRUT5 (mainly used)	HadCRUT4.6
In Figs.	figs. S2, S14	figs. S2, S15	figs. S2, S16	Figs. 1, 2, 3, 4 figs. S2, S4, S5, S7, S8, S9, S10	fig. S20
β_{GHG}	1.28±0.20	1.16±0.15	1.13±0.14	1.31±0.22	1.08±0.22
$\beta_{non-GHG}$	1.83±0.70	1.30±0.48	1.26±0.48	2.07±0.81	1.57±0.84
β_{nat}	1.51±0.19	1.52±0.19	1.51±0.19	1.56±0.21	1.32±0.32
β_{MEI}^1	0.048±0.001	0.017±0.001	0.039±0.001	0.057±0.002	0.062±0.001
β_{MEI}^2	0.016±0.000	0.017±0.001	0.000±0.000	0.006±0.002	0.028±0.002
β_{MEI}^3	0.043±0.001	0.038±0.000	0.039±0.000	0.041±0.002	0.025±0.002
τ_1	0	2	2	0	0
τ_2	1	2	3	6	7
τ_3	9	3	4	8	10
Mean R^2	0.87	0.87	0.88	0.88	0.86
Mean cor-rel. between ENSO & residuals	2.8E-17	6.8E-18	8.7E-17	3.2E-17	1.5E-17
Mean cor-rel. between estimate & observation	0.93	0.93	0.94	0.94	0.93

Table : Fitted coefficients for the statistical model (continued)

Corresponding figures and estimates	HadCRUT5 w/ NCEP index	HadCRUT5 w/ CTI	HadCRUT5 w/ BEST index	HadCRUT5 w/ Etminan forcing	HadCRUT5 w/ AR5 forcing
In Figs.	figs. S2, S11, S17	figs. S2, S12, S18	figs. S2, S13, S19	figs. S2, S21	figs. S2, S22
β_{GHG}	1.17±0.17	1.16±0.19	1.25±0.19	1.36±0.23	1.25± 0.20
$\beta_{non-GHG}$	1.42±0.69	1.40±0.70	1.82±0.73	2.18±0.82	1.96± 0.80
β_{nat}	0.84±0.30	0.91±0.34	1.66±0.22	1.64±0.21	1.49±0.18
β_{MEI}^1	0.035±0.002	0.068±0.003	0.054±0.002	0.057±0.002	0.057±0.002
β_{MEI}^2	0.016±0.002	0.032±0.003	0.029±0.002	0.006±0.002	0.006±0.002
β_{MEI}^3	0.021±0.002	0.035±0.003	0.018±0.002	0.040±0.002	0.041± 0.003
τ_1	6	3	0	0	0
τ_2	7	8	8	6	6
τ_3	8	11	10	8	8
Mean R^2	0.87	0.84	0.86	0.88	0.88
Mean cor- rel. between ENSO & residuals	1.3E-17	-8.7E-18	-6.2E-18	6.7E-18	8.5E-18
Mean cor- rel. between estimate & observation	0.93	0.92	0.92	0.94	0.94